

# Streaming patterns in Faraday waves

Nicolas Perinet<sup>1</sup>, Pablo Gutiérrez<sup>1</sup>, Héctor Urra<sup>2</sup>,  
Nicolás Mujica<sup>1</sup> and Leonardo Gordillo<sup>1,3†</sup>

<sup>1</sup>Departamento de Física, Facultad de Ciencias Físicas y Matemáticas, Universidad de Chile,  
Casilla 487-3, Santiago, Chile

<sup>2</sup>Instituto de Física, Pontificia Universidad Católica de Valparaíso, Avenida Brasil, Valparaíso,  
Casilla 2950, Chile

<sup>3</sup>Department of Chemical Engineering and Materials Science, University of Minnesota,  
Minneapolis, Minnesota 55455, USA

(Received ?; revised ?; accepted ?. - To be entered by editorial office)

Waves patterns in the Faraday instability have been studied for decades. Besides the rich dynamics that can be observed on the waves at the interface, Faraday waves hide beneath them an elusive range of flow patterns —or streaming patterns— which have not been studied in detail until now. The streaming patterns are responsible for a net circulation in the flow which are reminiscent of convection cells. In this article, we analyse these streaming flows by conducting experiments in a Faraday-wave setup. To visualize the flows, tracers are used to generate both trajectory maps and to probe the streaming velocity field via Particle Image Velocimetry (PIV). We identify three types of patterns and experimentally show that identical Faraday waves can mask streaming patterns that are qualitatively very different. Next we propose a three-dimensional model that explains streaming flows in quasi-inviscid fluids. We show that the streaming inside the fluid arises from a complex coupling between the bulk and the boundary layers. This coupling can be taken into account by applying modified boundary conditions in a three-dimensional Navier-Stokes formulation for the streaming in the bulk. Numerical simulations based on this theoretical framework show good qualitative and quantitative agreement with experimental results. They also highlight the relevance of three-dimensional effects in the streaming patterns. Our simulations reveal that the variety of experimental patterns is deeply linked to the boundary condition at the top interface, which may be strongly affected by the presence of contaminants along the surface.

**Key words:** Faraday waves, Pattern formation, Boundary layers

---

## 1. Introduction

In 1831, Michael Faraday published an article that became fundamental for the communities of fluid dynamics and nonlinear physics ([Faraday 1831](#)). It presented what nowadays is called the Faraday instability: the destabilisation of the free surface of a liquid into regular ripples after forcing its container to periodically vibrate in the vertical direction above some threshold. Periodical vibrations introduce a parametrical modulation to gravity, which creates regular stationary waves on the fluid surface that oscillate at half the forcing frequency (subharmonic waves) —the so called Faraday waves.

It may be surprising that such a seminal contribution was only an appendix in the 1831 article. The main content was devoted to the study of how solid particles move on

† lgordill@ing.uchile.cl

the surface of a vibrated elastic plate and why they tend to slowly cumulate in some specific regions. His aim was to better understand these patterns, also known as Chladni figures (Chladni, E.F.F. 1787). In this context, the first goal of the experiments included in the appendix was to change the density of the fluid surrounding the moving particles. Regardless the nature of the fluid, a key step to understand particle motion is to probe the velocity induced by the oscillatory motion of the fluid.

When considering Faraday waves, the velocity field has two clearly distinguishable components. First, there is an oscillatory part (see the illustrative images by [Wallet & Ruellan 1950](#), reproduced by [Van Dyke 1982](#)), whose importance was well known for surface waves since [Stokes \(1847\)](#) and whose linear and non-linear mechanisms have been deeply studied (see [Lamb, H. 2006](#); [Miles & Henderson 1990](#), and references therein). This early understanding was possible, in part, because viscous effects are not required to describe the oscillatory part with a high level of accuracy. Viscosity, however, is fundamental to describe the second component of the velocity field that becomes noticeable only after long times ([Longuet-Higgins 1953](#)). This time-independent velocity component was readdressed much more recently ([Douady 1990](#)), and followed by some theoretical descriptions ([Vega \*et al.\* 2001](#); [Martin \*et al.\* 2002](#); [Martin & Vega 2005](#)). Mean flows are crucial to understand advection of material inside the fluid over time scales longer than the period of container oscillation. Although the phenomenon is well known in acoustics (see [Riley 2001](#), and references therein), it has received little attention in the context of subharmonic waves. We will refer to these mean flows as Faraday streaming flows or, simply, streaming flows and concentrate our attention on them.

The already great impact of Faraday’s contribution can be even extended when considering the Faraday streaming flow. In particular, the motion produced by an oscillating fluid surface is a relevant open question. The dispersion of pollutants on the free surface of a flow involves several physical processes, including streaming flows. Various processes have been considered in recent experimental works ([Falkovich \*et al.\* 2005](#); [Sanli \*et al.\* 2014](#); [Gutiérrez & Aumaître 2016](#)), but a clear evaluation of the dominant effects is still lacking. On the other hand, Faraday waves have been proposed as a way to generate particulate films by deposition of heavy particles ([Wright & Saylor 2003](#)) and suspended templates of light particles ([Chen \*et al.\* 2014](#)), where again streaming flows are one key for the arising patterns. In another context, Faraday streaming flows are claimed to play an important role on the dynamics of localised structures, namely in their drift and interaction ([Vega \*et al.\* 2001](#); [Martin \*et al.\* 2002](#)). Because of the variety and relevance of its applications, a thorough study of the streaming flow (experimental, theoretical and numerical) is needed.

In this article, we perform a detailed analysis of the Faraday streaming flow that includes its experimental characterisation and a general theoretical development. By performing numerical simulations, we compare the experimental findings with the theory. In §2 we present the experiment. We briefly describe the setup and the Particle Image Velocimetry (PIV) measurements. Then, we focus on the observed mean flows. Section 3 concerns the theoretical development and includes a detailed extension to three dimensions of the Batchelor theory of oscillatory boundary layers ([Batchelor, G. K. 2000](#)). Special care was taken to present the theory in a self-consistent way. Our analysis ends with the boundary conditions that are used to perform simple numerical simulations in three dimensions whose results are presented in §4. Section 5 is devoted to discussion and conclusions.

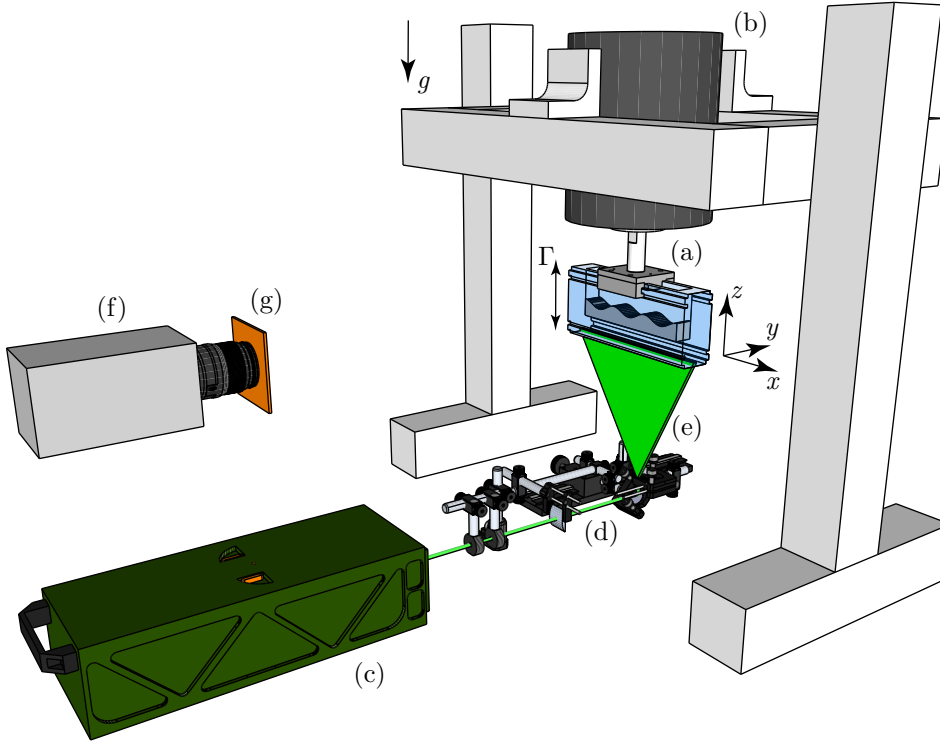


FIGURE 1. Experimental setup. A plexiglas trough (a) is vertically driven by an electromagnetic shaker (b). A double-pulsed laser (c) and an optical array (d) generates a light sheet (e) which passes through the trough. A high-speed camera (f) and a long-pass filter (g) acquires the images for PIV.

## 2. Measurements

### 2.1. Experimental setup

To run our experiments, we manufactured a plexiglas trough of  $L_x = 190.5$  mm long,  $L_y = 25.4$  mm broad and 69.6 mm deep. An aluminium piece attached to the top couples the trough to an electromechanical shaker (Dynamic Systems VTS-80). A function waveform generator (Rigol DG-1022) and a bipolar amplifier (NF HSA-4011) generate a sinusoidal signal with tuneable amplitude and frequency that properly feeds the shaker. The system's acceleration is precisely measured using an accelerometer (PCB Piezotronics 340A65) and a lock-in amplifier (Stanford Research SR830), synchronised with the shaker input signal. A second channel of the function waveform generator is used to create a synchronisation signal that triggers the imaging system at a programmable phase.

The upside configuration chosen for the experiment allows the system to be illuminated from the bottom, which is the only way to avoid undesired light refractions in Particle Image Velocimetry (PIV). A scheme of the setup is displayed in figure 1. Further details can be found in [Gordillo & Mujica \(2014\)](#). The PIV imaging system consists of a double-pulsed ND:YAG laser (Quantel Evergreen 70) and a high-speed camera (Phantom v641), properly synchronised. The laser beam passes through an optical system that projects a 2 mm-thick laser sheet into the trough. The optical system, mounted on a translational stage, allows to freely adjust the position of the illuminated plane in the  $y$  direction.

In all our runs, we filled the trough up to  $h = 20$  mm with an aqueous solution of

potassium bromide (KBr). The concentration, 13.7%, is such that the density of the solution matches the density of the seeding particles: Kanomax Fluostar,  $\varnothing = 15 \mu\text{m}$ ,  $\rho = 1.1 \text{ g/cm}^3$  (cf. tables for aqueous solutions in [Lide, D. R. 2004](#)). The seeding particles are fluorescent, a feature which is used to create sharp images. A long-pass filter placed in front of the objective lens filters off any reflection of the laser sheet on the free surface and only the light emitted by the fluorescent particles reaches the camera sensor. A small amount of wetting agent, 2 ml of Kodak Photoflo, is also added to the solution. The inclusion of this agent has been shown to improve wall wettability in this kind of system ([Wu \*et al.\* 1984](#)). Some ethyl alcohol (less than 1 ml) was used to previously dissolve the PIV seeding particles into water, avoiding the formation of clusters. The mixture of seeding particles was then kept in a syringe and added manually to the water until the concentration of particles in images is suitable for PIV (4 particles in an  $8 \times 8$ -pixels window, [Raffel, M. \*et al.\* 2007](#)).

Faraday waves are generated at the free surface of the fluid when the forcing acceleration  $\Gamma$  is increased above a threshold  $\Gamma_0$ , which is a function of the forcing frequency  $f$ . The waves are subharmonic, i.e. they oscillate at half the forcing frequency,  $f/2$ . The wavelength  $\lambda$  and wavenumber  $k = 2\pi/\lambda$  are related to the natural frequencies of the surface  $f_{m,n} = \omega_{m,n}/(2\pi)$  through the dispersion relation for closed basins

$$\omega_{m,n}^2 = gk \tanh kd. \quad (2.1)$$

The quantity  $k$  is the modulus of the wavenumber  $\mathbf{k} = (k_x, k_y) = (m\pi/L_x, n\pi/L_y)$  and  $m, n \in \mathbb{Z}$  are the number of nodes in each direction (for more details, cf. [Miles 1976](#)). For a forcing frequency  $f$  close to  $2f_{m,n}$ , the system responds with a wavelength given by (2.1). The sign of the detuning  $\Delta f = f/2 - f_{m,n}$  defines if the onset of the Faraday waves is subcritical ( $\Delta f < 0$ ) or supercritical ( $\Delta f > 0$ ), as shown by [Douady \(1990\)](#).

## 2.2. Observation of the streaming patterns

At first glance, the flow beneath the free surface is very simple: the fluid is carried from one crest to the neighbouring ones and then back through a cycle ([Van Dyke 1982](#)). However, particles do not come back exactly to the same position after each cycle. This fact can be easily observed when taking images stroboscopically. An overexposed image with strobe flashing, shows the slow tracks followed by particles after several cycles (see figure 2). These tracks will be referred to as *streaming patterns*, and their study, as the streaming flow or velocity field related to it, are the main goal of this work.

Despite the streaming patterns were observed indirectly by [Faraday \(1831\)](#) through the accumulation of particles on the bottom of the trough, the first visualisation is due to [Douady \(1990\)](#), who used Kalliroscope particles for this purpose.

The streaming patterns are generated by a secondary flow which is very small compared to the main oscillatory flow. In our experiments, the streaming velocity field is typically around 20 times weaker than the oscillatory velocity field ([Gordillo & Mujica 2014](#)). Despite its weakness, the streaming patterns can be easily observed using a strobe light as a consequence of the fact that the main flow (the dominant velocity signal) is periodical whereas the streaming one is mainly steady. Hence, the motion that particles undergo after a complete cycle due to the oscillatory field is zero and only the contribution of the streaming velocity field is observed. Notice that particles under the free surface of a standing wave, which is the case of the Faraday waves, have a Stokes drift ([Stokes 1847](#)) equal to zero after a complete cycle ([Gordillo 2012](#)).

The streaming patterns show also a weak dependence on the phase at which the images are captured. Naturally, the patterns are distorted with the deformation of the free surface at a given phase. For the sake of simplicity, all the quantitative measurements of the

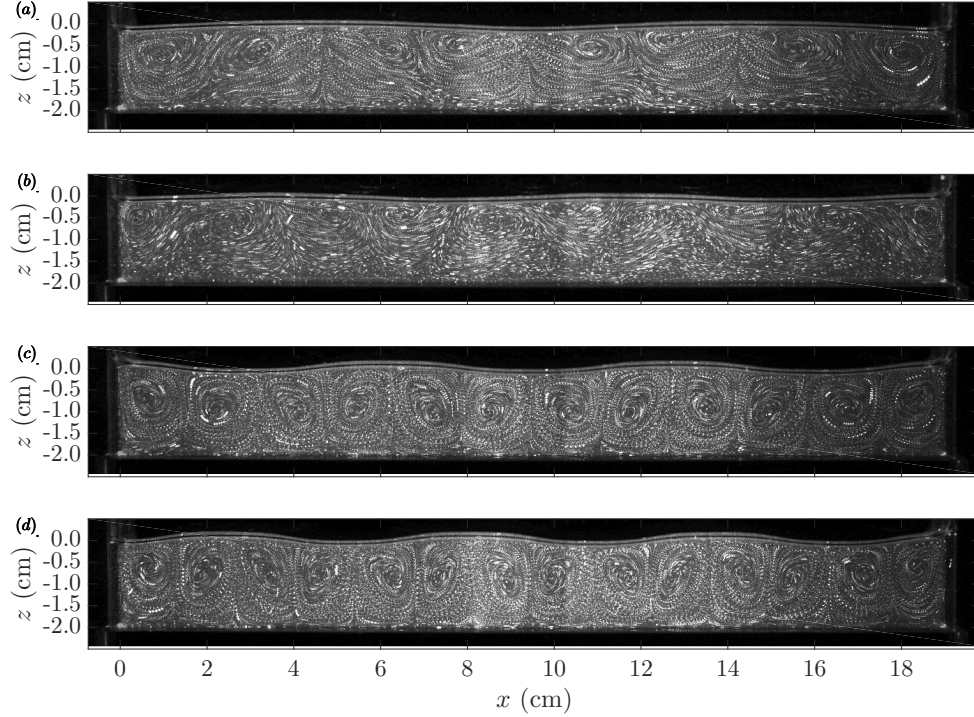


FIGURE 2. Streaming patterns beneath purely longitudinal Faraday waves for (a)  $f = 7.6$  Hz, (b)  $f = 8.9$  Hz, (c)  $f = 9.9$  Hz and (d)  $f = 10.8$  Hz in the midplane in the crosswise direction ( $y = L_y/2$ ). The images were obtained by strobe illumination. The number of nodes of the standing Faraday wave is respectively  $m = 4, 5, 6, 7$  ( $n = 0$ ).

streaming field were performed at the phase at which the free surface is flat and only on longitudinal Faraday waves (no crosswise component, i.e.  $n = 0$  in equation 2.1). For the same reason, all the measurements showed here are restrained to the midplane in the  $y$  direction.

The images in figure 2 also show that the structure of the streaming patterns is highly three-dimensional, even for Faraday waves with no crosswise component on the surface. Particles may enter and exit the illuminated plane, which explains the observed spiral trajectories followed by the particles.

### 2.3. Measurement protocol

To characterise the dependence of the streaming patterns on the amplitude and the frequency, we performed several experimental runs. The protocol was automatized using Matlab, which controlled, via several interfaces (GPIB, USB, RS232 and Ethernet) all the devices involved in the experiment. Each set of measurements analysed a single forcing frequency. The protocol was the following: First, the amplitude was increased until stationary Faraday waves with large-amplitude emerge. A downward-ramp scheme in amplitude was then followed: For each amplitude, we record a first series of 36 images, which completed a cycle, to determine the shape of the interface in terms of the phase (or time). Immediately after, the shape of the free surface was detected using a standard algorithm for edge detection. After the flat-state phase was determined, the synchronisation signal was shifted and a second run consisting of 64 stroboscopic flat-state images was

---

label	$f$ (Hz)	number of nodes ( $m$ )	nonlinear behaviour	observed types
a	7.6	4	subcritical	II
b	8.9	5	subcritical	III
c	9.9	6	subcritical	I, III
d	9.95	6	supercritical	I, III
e	10.8	7	subcritical	I
f	10.85	7	supercritical	I
g,h,i,j	10.8	7	subcritical	I, II, III

---

TABLE 1. Set of measurements for the streaming patterns. Each line corresponds to a ramp in amplitude. The set includes four different wavelengths. Faraday waves destabilise through subcritical or supercritical bifurcations depending on the frequency detuning. Both subcritical and supercritical behaviours are explored. The last column shows the observed type of streaming pattern.

---

recorded. Measurements were done cyclically every four minutes, following the downward ramp until the Faraday waves on the surface vanished.

In Table 1, we display a list of the experiments performed. The runs include different frequencies and different wavenumbers. We also studied different nonlinear scenarios, i.e. subcritical and supercritical behaviour. Measurement ramps lasted between 1 to 4 hours, depending on the initial amplitude and the ramp step size.

#### 2.4. Experimental results

Our sequences of images were processed by means of two different techniques. In a very simple way, the sequences can be used to detect the trajectories followed by the seed particles. A synthetical over-exposed image is obtained by maximising the grey value of each pixel along several frames. This is actually how the images in figure 2 were obtained. This strategy allows to fast probe the streaming patterns and provides a powerful qualitative tool to analyse the data on the run. The second technique is PIV, which provides precise quantitative data. For this purpose, each sequence of images was analysed using our own PIV code. After preparing masks and background subtraction, we used time-averaging in the correlation-function space to improve the signal-to-noise ratio (Meinhart *et al.* 2000). This allows us to obtain neat velocity fields with a high spatial resolution ( $8 \times 8$ -pixel window size, equivalent to  $0.64 \times 0.64 \text{ mm}^2$  resolution) and no spatial averaging (0% overlapping).

Figures 2 and 3 show respectively the streaming pattern and the velocity field ( $u, w$ ) in the  $(x, z)$ -plane for four different forcing frequencies. The presented cases are a good representation of the whole set of collected data. In all our measurements, we observe: (i) a sequence of counter-rotating structures with a wavelength equal to half the free surface wavelength, (ii) that velocity field strength decreases with depth, and (iii) the fluid is pushed downward at the free-surface antinodes and upward at the nodes. However there are clear differences between the flow structures in the subfigures presented in figures 2 or 3. Based on our results and qualitative criteria, we identify three types of streaming patterns:

- Type I: sequence of counter-rotating rolls (inset c-d);
- Type II: sequence of moustache-shaped swirls (inset a);
- Type III: irregular patterns (inset b).

Although only type I and II show ordered structures, type III displays well-shaped rolls



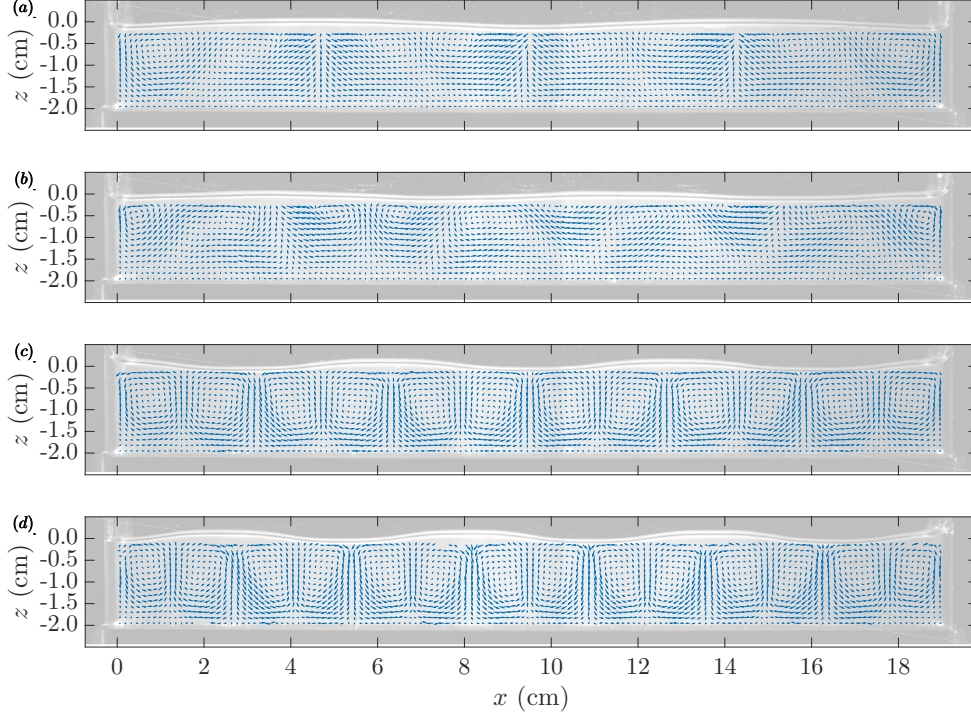


FIGURE 3. Velocity field of the streaming patterns shown in figure 2 (increasing wavenumber from top to bottom). The background shows the shape of the interface 20 ms after the flat phase. Insets (a), (c) and (d) show ordered patterns with a spatial period equal to the half of the surface waves. Inset (b) shows a distorted streaming pattern.

next to the lateral walls at  $x = 0$  and  $x = L_x$ . Types I and II share another common feature: both display squeezed counter-rotating structures at the bottom.

To illustrate quantitatively the classification described previously, we chose two quantities that characterise the state of the system. The first one is the amplitude  $\zeta$  of the Faraday wave and is used to quantify the state of the free-surface. This quantity can be obtained from the sequence of images used for determining the flat state (see §2.3). As second parameter, intended to represent the state of the flow, we chose the amplitude (along the  $x$  coordinate) of the vertically averaged velocity  $w$ , i.e.

$$\hat{w} \equiv \max_{x \in D} \left| \frac{1}{d} \int_{-d}^0 dz w(x, y = b/2, z) \right|.$$

Since the lateral walls induce strong coherent structures for all the types, the domain  $D$  is chosen such that the first and last roll are removed, i.e.  $D : [\lambda/4, L_x - \lambda/4]$ . The quantity  $\hat{w}$  can be easily obtained from PIV data (the discretised  $dz$  is 0.64 mm). Averaging along  $z$  cancels noise induced by PIV detection.

The two chosen quantities are plotted against each other in figure 4 for all our measurements. For values of  $\zeta$  below some threshold  $\zeta_0 \approx 1.5$  mm,  $\hat{w}$  values remains almost equal to zero, which is related to the absence of periodic structures. Beyond this threshold,  $\hat{w}$  bifurcates into two branches, each containing a large amount of collapsed measurement points. All type-I streaming patterns collapse to the upper branch, while type-II patterns collapse to the lower one. The upper branch displays  $\hat{w}$ -values twice as strong as than the

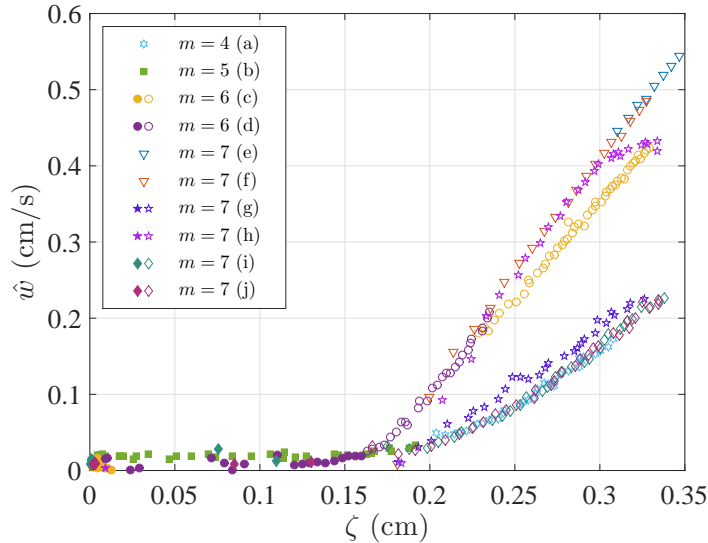


FIGURE 4. Bifurcation diagram for streaming patterns. The diagram shows all the collected data which collapse into two branches. The upper branch contains Type I streaming patterns (roll structures) and the lower one, Type II patterns. Type III (filled symbols) patterns can only be observed for very low amplitudes.

lower one. Type-III patterns can be observed only for low  $\hat{w}$  values, which gives a hint to understand their existence. A reasonable explanation is that the coherent periodic structures induced by the Faraday waves are so weak that they compete with weak parasite large-scale eddies. The latter are presumably generated by surface tension effects and persist for long times, even after the vibration is switched off).

Figure 4 reveals that subcritical or supercritical behaviour has not any relevant effect on streaming patterns: series (c) and (d) form a continuous line for  $m = 6$ ; the same stands for series (e) and (f), where  $m = 7$ . More strikingly, Type I and II patterns may emerge regardless the value of  $\lambda$ . The evidence for  $m = 7$  is remarkable because both types are observed with the same forcing parameters: type I, runs (e),(f) and (h) and type II, runs (i) and (j). The mixture in the trough was the same and most of the runs were taken during the same day. We could not find a way to choose which streaming-flow pattern (I or II) was going to be selected during an experiment: the system spontaneously chooses one and keeps it until the wave on the surface vanishes. Multi-stability of viscous modes have been observed in other flows, *e.g.* Coles (1965) observed more than 20 different states in the Taylor-Couette flow under the same forcing parameters .

As a closing for this section, we would like to readdress the effect of the streaming patterns at long timescales on particles in the liquid. Consider a particle subjected to the flow under Faraday waves. Besides the oscillating forces due to the fast oscillating velocity field, our particle is subjected to a viscous steady force due to the streaming flow. Hence, at long timescales, the particle will be slowly drifted by this force until it reaches a stagnation point. Particles heavier than the fluid will accumulate at stagnation points at the bottom of the trough, creating the heaps observed by Faraday in his seminal experiments. Particles lighter than the fluid, will float at the free surface, and accumulate into *rafts* as has been shown in experiments by Falkovich *et al.* (2005) and Sanli *et al.* (2014). The streaming flows are thus a relevant extra ingredient to understand the motion induced on particles on Faraday waves. A step forward is to build a theory that explains



the emergence of the streaming patterns observed in our experiments. The next section is devoted to this task.

### 3. Theory

We consider a three-dimensional infinite layer of an incompressible and viscous fluid (density  $\rho$  and kinematic viscosity  $\nu$ ) delimited at its bottom by an impermeable flat wall. The flow far from the wall is tangent to the wall and periodic in time. Our purpose is to determine the stationary component, or streaming, due to this periodic flow. The streaming is the result of a complex mechanism that couples the flows inside the bulk (far from the walls) and at the boundary layers (near the walls). The coupling can be split in three intermediate mechanisms:

- (a) the oscillatory flow in the bulk induces an oscillating boundary layer,
- (b) the oscillating boundary layer exerts a feedback on the bulk flow whose steady component originates the streaming,
- (c) the streaming is diffused into the bulk due to a viscous process.

In §3.1 we present an extension of Batchelor's two-dimensional model for oscillatory flows (see Batchelor, G. K. 2000, pp. 353-364) to three dimensions whose basis is two-fold: the length scale separation between the viscous boundary layer and the bulk flows; and the emergence of steady terms due to nonlinear convective term at the boundary layer. For the sake of clarity, we outline here our theoretical framework. First, in §3.1.1, we pose the generic problem of an oscillating flow near a rigid wall. In §3.1.2 we determine the equations in both the boundary layer and the bulk. Starting from the hypothesis of weak quasi-inviscid waves, we define two small parameters:  $\gamma$ , the ratio of the boundary layer thickness to the typical length scale the bulk flow and  $\beta$ , the ratio of the period of the oscillating flow to the convective time scale. Navier-Stokes equations are accordingly expanded in powers of  $\gamma$  and  $\beta$  inside the boundary layer as well as in the bulk. Order by order, equations are truncated, solved and matched at the junction. At dominant order (see §3.1.3), an oscillatory boundary layer is obtained due to the oscillating field at the bulk [mechanism (a)]. Higher-order equations in  $\beta$  and  $\gamma$  yield an equation for the streaming flow inside the boundary layer (see §3.1.4). This streaming flow induces a streaming velocity at the junction [mechanism (b)], which can be identified as a *matched* boundary condition at the wall for the bulk streaming flow. Finally, we show in §3.2 that the streaming flow in the bulk can be computed by solving an independent Navier-Stokes equations for the streaming velocities, with the aforementioned matched boundary conditions. The result is the diffusion of the streaming from the boundaries into the bulk [mechanism (c)]. Finally, our theoretical framework is applied to find the matched streaming boundary conditions for Faraday waves in §3.3, which are required to solve the streaming Navier-Stokes equations in §4.

#### 3.1. Three-dimensional streaming due to an oscillatory boundary layer

##### 3.1.1. External oscillatory field

We denote a local coordinate system  $(x, y, z)$  as shown in figure 5(a);  $u$ ,  $v$  and  $w$  are the components of the velocity along the  $x$ ,  $y$  and  $z$  directions, respectively. The local coordinates are chosen such that the  $z$  axis is normal to the wall and points towards the bulk. The  $z$ -domain is split into two subdomains: an inner region which comprises the boundary layer at the vicinity of the wall and an outer region extending beyond the boundary layer. The fields inside the boundary layer are denoted  $u$ ,  $v$ ,  $w$  and  $p$ , standing for the components of the velocity and the pressure. Outside the boundary layer, the

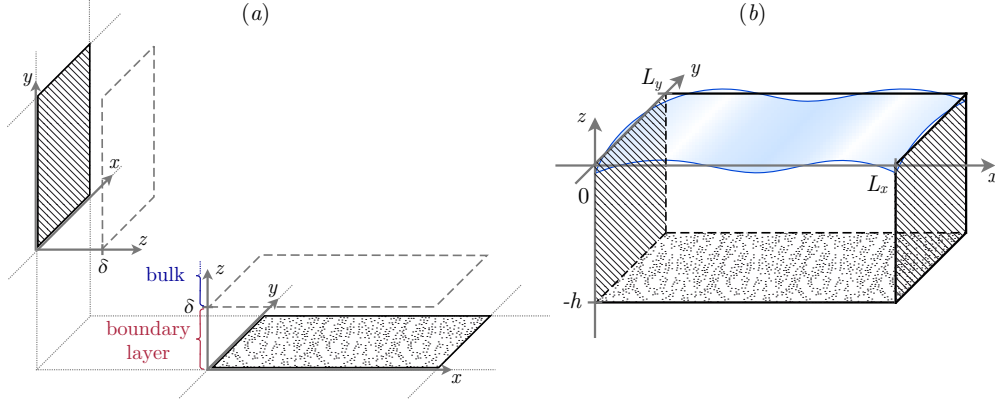


FIGURE 5. (a) Local coordinate systems on two walls of the container. The colored surfaces represent parts of the walls far from the edges of the domain. The grey parallelograms show the limit of the boundary layer at the distance  $\delta$  from the walls. (b) Definition of the domain containing the fluid for numerical simulations.

outer flow is denoted by the fields  $\underline{u}$ ,  $\underline{v}$ ,  $\underline{w}$  and  $\underline{p}$ . The outer flow is externally imposed, assumed to be tangent at  $z = 0$ , and given by the general form

$$(\underline{u}, \underline{v}, \underline{w}) = \text{Re} \left\{ (U_0(x, y, z), V_0(x, y, z), W_0(x, y, z)) e^{i\omega t} \right\}, \quad (3.1)$$

$$\underline{w}|_{z=0} = 0.$$

The length scale of variations in the three directions  $x$ ,  $y$  and  $z$  are assumed to be of order  $L$ . As we will see, this outer flow induces inside the boundary layer a motion influenced by viscous stresses.

### 3.1.2. Boundary layer equations

We place ourselves inside the oscillating boundary layer and consider the full Navier-Stokes equations for an incompressible flow:

$$\begin{aligned} \partial_t u + u \partial_x u + v \partial_y u + w \partial_z u &= -\frac{1}{\rho} \partial_x p + \nu \partial_{xx} u + \nu \partial_{yy} u + \nu \partial_{zz} u, \\ \partial_t v + u \partial_x v + v \partial_y v + w \partial_z v &= -\frac{1}{\rho} \partial_y p + \nu \partial_{xx} v + \nu \partial_{yy} v + \nu \partial_{zz} v, \\ \partial_t w + u \partial_x w + v \partial_y w + w \partial_z w &= -\frac{1}{\rho} \partial_z p + \nu \partial_{xx} w + \nu \partial_{yy} w + \nu \partial_{zz} w, \\ \partial_x u + \partial_y v + \partial_z w &= 0. \end{aligned} \quad (3.2)$$

We rewrite the involved physical fields in terms of dimensionless quantities:

$$\begin{aligned} u &= U_0 u', & v &= U_0 v', & w &= U_0 w', & p &= \rho \omega L U_0 p', \\ \partial_x &= \frac{1}{L} \partial_{x'}, & \partial_y &\sim \frac{1}{L} \partial_{y'}, & \partial_z &\sim \frac{1}{\delta} \partial_{z'}, & \partial_t &\sim \omega \partial_{t'}. \end{aligned} \quad (3.3)$$

Here, the length scale  $\delta$  is defined as  $\sqrt{2\nu/\omega}$  and represents the extent of the boundary layer. Based on this, we define two dimensionless parameters  $\gamma$  and  $\beta$ :

$$\gamma \equiv \frac{\delta}{L} \ll 1, \quad \beta \equiv \frac{U_0}{\omega L} \ll 1. \quad (3.4)$$

The quantity  $\gamma$  represents the ratio between the boundary layer extent  $\delta$  and the outer-flow length scale  $L$  while  $\beta$  is the ratio between the period of the oscillating flow and the convective timescale (a low  $\beta$  implies weak convection). Using the previous definitions, the set of equations in (3.2) are hence reduced to

$$\begin{aligned} \partial_t(u, v) + \beta \left( u\partial_x + v\partial_y + \frac{1}{\gamma}w\partial_z \right) (u, v) &= -(\partial_x, \partial_y)p + \frac{1}{2}[\gamma^2(\partial_{xx} + \partial_{yy}) + \partial_{zz}](u, v), \\ \gamma\partial_t w + \beta\gamma \left( u\partial_x w + v\partial_y w + \frac{1}{\gamma}w\partial_z w \right) &= -\partial_z p + \frac{1}{2}[\gamma^3(\partial_{xx} + \partial_{yy}) + \gamma\partial_{zz}]w, \\ \gamma(\partial_x u + \partial_y v) + \partial_z w &= 0, \end{aligned} \quad (3.5)$$

where primes have been omitted for simplicity. We now expand the fields in powers of  $\beta$  and  $\gamma$ :

$$\begin{bmatrix} u \\ v \\ w \\ p \end{bmatrix} = \begin{bmatrix} u_0 \\ v_0 \\ 0 \\ p_0 \end{bmatrix} + \beta \begin{bmatrix} u_1 \\ v_1 \\ w_1 \\ p_1 \end{bmatrix} + \gamma \begin{bmatrix} \tilde{u}_1 \\ \tilde{v}_1 \\ \tilde{w}_1 \\ \tilde{p}_1 \end{bmatrix} + \dots \quad (3.6)$$

This expansion is plugged into (3.5), providing a hierarchy of equations of powers of  $\beta$  and  $\gamma$ †. The first equations of the hierarchy are:

$$\mathcal{O}(1) : \begin{cases} \partial_t(u_0, v_0) = -(\partial_x, \partial_y)p_0 + \frac{1}{2}\partial_{zz}(u_0, v_0), \\ \partial_z p_0 = 0 \end{cases} \quad (3.7)$$

$$\mathcal{O}(\gamma) : \begin{cases} \partial_z \tilde{p}_1 = 0, \\ \partial_x u_0 + \partial_y v_0 + \partial_z \tilde{w}_1 = 0 \end{cases} \quad (3.8)$$

$$\mathcal{O}(\beta) : \begin{cases} \partial_t(u_1, v_1) = -(u_0\partial_x + v_0\partial_y + \tilde{w}_1\partial_z)(u_0, v_0) - (\partial_x, \partial_y)p_1 + \frac{1}{2}\partial_{zz}(u_1, v_1), \\ \partial_z p_1 = 0, \\ \partial_z w_1 = 0. \end{cases} \quad (3.9)$$

A similar analysis can be performed for the outer flow. In that case, the rescaling rules from (3.3) apply except for  $\partial_z = \frac{1}{\delta}\partial_{z'}$ , which should be replaced by  $\partial_z \approx \frac{1}{L}\partial_{z'}$ . Likewise, a zero-th order term  $\underline{w}_0$  should be included in the expansion in powers of  $\beta$  and  $\gamma$  (3.6)‡. Order by order, it follows that

$$\mathcal{O}(1) : \begin{cases} \partial_t(\underline{u}_0, \underline{v}_0, \underline{w}_0) = -(\partial_x, \partial_y, \partial_z)\underline{p}_0, \\ \partial_x \underline{u}_0 + \partial_y \underline{v}_0 + \partial_z \underline{w}_0 = 0, \end{cases} \quad (3.10)$$

$$\mathcal{O}(\beta) : \partial_t(\underline{u}_1, \underline{v}_1, \underline{w}_1) = (-\underline{u}_0\partial_x - \underline{v}_0\partial_y - \underline{w}_0\partial_z)(\underline{u}_0, \underline{v}_0, \underline{w}_0) - (\partial_x, \partial_y, \partial_z)\underline{p}_1. \quad (3.11)$$

To find asymptotically uniform solutions in the whole domain, the final step is to match the fields at the junction (Bender, C. M. & Orszag, S. A. 1999). From a mathematical point of view, this is equivalent to impose that the fields in the inner flow  $(u, v, w, p)$  eval-

† Since  $\beta$  and  $\gamma$  have a priori different and unknown orders of magnitude, identifications as  $\beta^p = \gamma^q$  or subsequent simplifications are not consistent.

‡ The normal velocity condition  $\underline{w}_0 = 0$  is required only at  $z = 0$ .

uated in the limit  $z' \rightarrow \infty$  are equal to those in the outer flow,  $(\underline{u}_1, \underline{v}_1, \underline{w}_1, \underline{p}_1)$  evaluated in limit  $z \rightarrow 0$ .

### 3.1.3. Zeroth order: The oscillatory boundary layer

The equations for the dominant variables  $u_0, v_0$  and  $p_0$  are given by (3.7). Notice that including a  $w_0$  term in the expansion (3.6), yields  $\partial_z w_0 = 0$  at leading order, which requires  $w_0 = 0$  to satisfy the non-slip boundary condition at  $z = 0$ . On the other hand, the  $z$ -independence of  $p_0$  implies that the pressure is constant across the boundary layer. The matching condition for the pressure becomes trivial and (3.10) can be used to eliminate the pressure from the unknowns. Accordingly,  $u_0$  relates to  $\underline{u}_0$  as follows

$$\partial_t (u_0, v_0) = \partial_t (\underline{u}_0, \underline{v}_0) + \nu \partial_{zz} (u_0, v_0). \quad (3.12)$$

The equation (3.12) with the prescribed boundary conditions admits the solution

$$\begin{aligned} u_0(x, y, z, t) &= \text{Re} \{ U_0(x, y) e^{i\omega t} (1 - e^{-\alpha z}) \}, \\ v_0(x, y, z, t) &= \text{Re} \{ V_0(x, y) e^{i\omega t} (1 - e^{-\alpha z}) \}, \end{aligned} \quad (3.13)$$

where  $\alpha = (1 + i)$ . Notice that the boundary layer, in this approximation oscillates at the same frequency as the bulk fields. In the case  $U_0(x, y, z) = U_0, V_0(x, y, z) = V_0$  and  $W_0(x, y, z) = 0$ , this solution reduces to the oscillatory boundary layer found by Stokes (1851), which are an exact solution of the Navier-Stokes equation.

### 3.1.4. The induced streaming

From the equations (3.9), it can be easily shown that  $p_1$  and  $w_1$  follow the same rules as  $p_0$  and  $w_0$ . Up to this point, we notice that the first non-trivial term of the expansion for  $w$  is proportional to  $\gamma$ , which means that  $w$  scales as  $\delta U_0/L$  and not as  $U_0$ . Remarkably, although at zeroth order  $w$  vanishes, at higher order,  $w$  induces a flow inside the boundary layer as will be shown in the following calculations. From the divergence equation in (3.8) and the variables  $u_0$  and  $v_0$  computed in (3.13), we deduce  $\tilde{w}_1$ , whose expression,

$$\tilde{w}_1(x, y, z, t) = - \int_0^z \text{Re} \{ (\partial_x U_0 + \partial_y V_0) e^{i\omega t} (1 - e^{-\alpha z}) \} dz, \quad (3.14)$$

consistently satisfies the no-slip boundary condition at the wall  $\tilde{w}_1 = 0$ . Since  $p_1$  is also constant across the boundary layer,  $p_1$  equals  $\underline{p}_1$  all along it, which is used to link the first equation in (3.9) and 3.11:

$$\begin{aligned} \partial_t u_1 + u_0 \partial_x u_0 + v_0 \partial_y u_0 + \tilde{w}_1 \partial_z u_0 &= \partial_t \underline{u}_1 + \underline{u}_0 \partial_x \underline{u}_0 + \underline{v}_0 \partial_y \underline{u}_0 + \frac{1}{2} \partial_{zz} u_1, \\ \partial_t v_1 + u_0 \partial_x v_0 + v_0 \partial_y v_0 + \tilde{w}_1 \partial_z v_0 &= \partial_t \underline{v}_1 + \underline{u}_0 \partial_x \underline{v}_0 + \underline{v}_0 \partial_y \underline{v}_0 + \frac{1}{2} \partial_{zz} v_1, \\ w_1 &= 0. \end{aligned} \quad (3.15)$$

The streaming is extracted from (3.15), by averaging over one period of oscillation  $T = 2\pi/\omega$ . The nonlinear terms provide components that oscillate at the frequency  $2\omega$  and some that are steady. To match the nonlinear terms of (3.15),  $u_1, v_1, \underline{u}_1$  and  $\underline{v}_1$  are assumed to have the generic form

$$\mathcal{A}(x, y, z) e^{i2\omega t} + \mathcal{B}(x, y, z) + \mathcal{A}^*(x, y, z) e^{-i2\omega t}, \quad (3.16)$$

where  $*$  denotes the complex conjugate operator,  $\mathcal{A}$  and  $\mathcal{A}^*$  are the oscillating components of the fields and  $\mathcal{B}$  is stationary and responsible for the streaming in the bulk. Then we focus on  $\mathcal{B}$ . We define the temporal average  $\langle f(t) \rangle$  of a function  $f(t)$  as  $\langle f(t) \rangle =$

$\frac{1}{T} \int_0^T f(t) dt$ , where  $T = 2\pi/\omega$ . Taking the generic form of  $u_1$  (3.16), we can easily deduce that  $\langle \partial_t u_1 \rangle = 0$  as well as  $v_1$ ,  $\underline{u}_1$  and  $\underline{v}_1$ . The system (3.15) then simplifies to a system of ordinary differential equations (ODEs) in  $\langle u_1 \rangle$ ,  $\langle v_1 \rangle$  and  $\langle w_1 \rangle$  after averaging:

$$\begin{aligned} \frac{1}{2} \partial_{zz} \langle u_1 \rangle &= \langle u_0 \partial_x u_0 \rangle + \langle v_0 \partial_y u_0 \rangle + \langle \tilde{w}_1 \partial_z u_0 \rangle - \langle \underline{u}_0 \partial_x \underline{u}_0 \rangle - \langle \underline{v}_0 \partial_y \underline{v}_0 \rangle, \\ \frac{1}{2} \partial_{zz} \langle v_1 \rangle &= \langle u_0 \partial_x v_0 \rangle + \langle v_0 \partial_y v_0 \rangle + \langle \tilde{w}_1 \partial_z v_0 \rangle - \langle \underline{u}_0 \partial_x \underline{v}_0 \rangle - \langle \underline{v}_0 \partial_y \underline{u}_0 \rangle, \\ \langle w_1 \rangle &= 0. \end{aligned} \quad (3.17)$$

Starting from here we focus on  $\langle u_1 \rangle$  only, since  $\langle v_1 \rangle$  can be found by analogy. The temporal averages of each term in (3.17) are given below:

$$\begin{aligned} \langle u_0 \partial_x u_0 \rangle &= \frac{1}{4} (1 - e^{-\alpha z}) (1 - e^{-\alpha^* z}) \partial_x (U_0 U_0^*), \\ \langle v_0 \partial_y u_0 \rangle &= \frac{1}{4} (1 - e^{-\alpha z}) (1 - e^{-\alpha^* z}) (V_0 \partial_y U_0^* + V_0^* \partial_y U_0), \\ \langle \tilde{w}_1 \partial_z u_0 \rangle &= -\frac{1}{2} \text{Re} \left\{ (\partial_x U_0 + \partial_y V_0) U_0^* \left[ \left( z \alpha^* - \frac{\alpha^*}{\alpha} \right) e^{-\alpha^* z} + \frac{\alpha^*}{\alpha} e^{-(\alpha + \alpha^*) z} \right] \right\}, \\ \langle \underline{u}_0 \partial_x \underline{u}_0 \rangle &= \frac{1}{4} \partial_x (U_0 U_0^*), \\ \langle \underline{v}_0 \partial_y \underline{v}_0 \rangle &= \frac{1}{4} (V_0 \partial_y U_0^* + V_0^* \partial_y U_0). \end{aligned} \quad (3.18)$$

Summing all these terms together we establish the ODE that satisfies  $\langle u_1 \rangle$

$$\partial_{zz} \langle u_1 \rangle = G_1(z) \text{Re} (U_0 \partial_x U_0^* + V_0 \partial_y U_0^*) + \text{Re} [G_2(z) (\partial_x U_0 + \partial_y V_0) U_0^*], \quad (3.19)$$

where

$$\begin{aligned} G_1(z) &= (1 - e^{-\alpha z})(1 - e^{-\alpha^* z}) - 1, \\ G_2(z) &= - \left[ \left( z \alpha^* - \frac{\alpha^*}{\alpha} \right) e^{-\alpha^* z} + \frac{\alpha^*}{\alpha} e^{-(\alpha + \alpha^*) z} \right]. \end{aligned} \quad (3.20)$$

For simplicity in what follows, the right-hand side of (3.19) is denoted  $G(x, y, z)$ . The associated boundary conditions are

$$\begin{aligned} \langle u_1 \rangle|_{z=0} &= 0, \\ \partial_z \langle u_1 \rangle|_{z=\infty} &= 0, \end{aligned} \quad (3.21)$$

from which we compute the streaming component:

$$\langle u_1 \rangle = \int_0^z \int_\infty^{z'} G(x, y, z'') dz'' dz'. \quad (3.22)$$

At the junction, *i.e.* in the limit  $z \rightarrow \infty$ ,  $\langle u_1 \rangle$  must match  $\langle \underline{u}_1 \rangle$  in the limit  $z \rightarrow 0$ , hence

$$\begin{aligned} \lim_{z \rightarrow 0} \langle \underline{u}_1 \rangle = \lim_{z \rightarrow \infty} \langle u_1 \rangle &= - \left[ \frac{1}{(\alpha + \alpha^*)^2} - \frac{\alpha^2 + \alpha^{*2}}{\alpha^2 \alpha^{*2}} \right] \text{Re} (U_0 \partial_x U_0^* + V_0 \partial_y U_0^*) \\ &\quad + \text{Re} \left\{ \left[ \frac{2}{\alpha^{*2}} - \frac{1}{\alpha \alpha^*} + \frac{\alpha^*}{\alpha(\alpha + \alpha^*)^2} \right] (\partial_x U_0 + \partial_y V_0) U_0^* \right\}. \end{aligned} \quad (3.23)$$

The latter equation can be replaced in (3.6) to obtain  $(u, v, w)$ , which in turn can be rescaled back to the original physical variables via (3.4) and (3.3). This yields

$$\begin{aligned} \lim_{z \rightarrow 0} \langle \underline{u} \rangle = & -\frac{1}{4\omega} [\text{Re}(U_0 \partial_x U_0^* + V_0 \partial_y U_0^*)] \\ & + \frac{1}{8\omega} [(3i - 2)(\partial_x U_0 + \partial_y V_0)U_0^* - (3i + 2)(\partial_x U_0^* + \partial_y V_0^*)U_0]. \end{aligned} \quad (3.24)$$

It must be noted that the analysis at order  $\gamma$  is similar to that of (3.7) and yields oscillating solutions which cancel when temporally averaged. Hence, only the perturbation at order  $\beta$ , which contains nonlinearities, generates the streaming. In other words, the streaming emerges from the nonlinear nature of the convective term of Navier-Stokes equation near the rigid wall.

The  $v$  component of the streaming can be calculated straightforwardly by applying the permutations  $U_0 \leftrightarrow V_0$  and  $\partial_x \leftrightarrow \partial_y$ . This leads to

$$\begin{aligned} \lim_{z \rightarrow 0} \langle \underline{v} \rangle = & -\frac{1}{4\omega} [\text{Re}(U_0 \partial_x V_0^* + V_0 \partial_y V_0^*)] \\ & + \frac{1}{8\omega} [(3i - 2)(\partial_x U_0 + \partial_y V_0)V_0^* - (3i + 2)(\partial_x U_0^* + \partial_y V_0^*)V_0]. \end{aligned} \quad (3.25)$$

The equations (3.24) and (3.25) describe the streaming at the junction of the bulk and the boundary layer. In vector notation, we rewrite the latter expression as:

$$\lim_{z \rightarrow 0} \langle \underline{\mathbf{u}} \rangle = -\frac{1}{4\omega} \{ \text{Re} [(\mathbf{U}_0^* \cdot \nabla) \mathbf{U}_0 + 2\mathbf{U}_0^* \nabla \cdot \mathbf{U}_0] + 3\text{Im}(\mathbf{U}_0^* \nabla \cdot \mathbf{U}_0) \} \quad (3.26)$$

where  $\mathbf{U}_0 = (U_0, V_0, 0)$  and the component of  $\mathbf{U}_0$  normal to the wall is uniformly 0 so neither  $w$  nor any of its derivatives appear in (3.26).

A simpler expression can be obtained for flows that oscillate at the same phase in both directions, *i.e.*  $\mathbf{U}_0 = \mathcal{U}_0(x, y)e^{i\Theta(x, y)}$ , where the magnitude  $\mathcal{U}_0$  is a real vector (with zero  $z$ -component) and the phase  $\Theta$  is a real scalar:

$$\lim_{z \rightarrow 0} \langle \underline{\mathbf{u}} \rangle = -\frac{1}{4\omega} [(\mathcal{U}_0 \cdot \nabla) \mathcal{U}_0 + 2\mathcal{U}_0 \nabla \cdot \mathcal{U}_0 + 3\mathcal{U}_0 (\mathcal{U}_0 \cdot \nabla) \Theta]. \quad (3.27)$$

The case of the two-dimensional streaming flow found by Batchelor, G. K. (2000) is

$$\lim_{z \rightarrow 0} \langle \underline{u} \rangle = -\frac{3}{4\omega} (\mathcal{U}_0 \partial_x \mathcal{U}_0 + \mathcal{U}_0^2 \partial_x \Theta), \quad (3.28)$$

which consistently matches the three-dimensional one, (3.27), when one of the two components of  $\mathbf{U}_0$  is imposed to be 0.

### 3.2. Streaming in the bulk

The final step is to determine how the streaming due to the boundary layers induces a streaming in the bulk. For this purpose, consider the general Navier-Stokes equation for the bulk in a comoving frame of reference,

$$\partial_t \underline{\mathbf{u}} + (\underline{\mathbf{u}} \cdot \nabla) \underline{\mathbf{u}} = -\frac{1}{\rho} \nabla \underline{p} + a(t) \hat{\mathbf{k}} + \nu \nabla^2 \underline{\mathbf{u}}, \quad (3.29)$$

where  $a(t) = -g + \Gamma \cos \omega t$  is the vertical acceleration of the system.† To simplify the notation, we omit the underline. We decompose the velocity and pressure field into oscil-

† Capillary terms can also be included.



latory and steady terms:  $\mathbf{u}(\mathbf{x}, t) = \tilde{\mathbf{u}}(\mathbf{x}, t) + \bar{\mathbf{u}}(\mathbf{x})$  and  $p(\mathbf{x}, t) = \tilde{p}(\mathbf{x}, t) + \bar{p}(\mathbf{x})$ . For most Faraday waves experiments, since  $\lambda, h, L_x, L_y \gg \delta$  the flow under the waves is potential at leading order, i.e.  $\tilde{\boldsymbol{\omega}} = \nabla \times \tilde{\mathbf{u}}(\mathbf{x}, t) = 0$ , where  $\boldsymbol{\omega}$  is the vorticity. Linear and nonlinear solutions for the oscillatory part have been widely analyzed in the literature (see [Miles 1993](#), and references therein).

The convective term in (3.29) can be written in terms of  $\boldsymbol{\omega}$ . It can be easily shown that  $(\mathbf{u} \cdot \nabla) \mathbf{u} = \nabla \left( \frac{1}{2} \tilde{u}^2 + \frac{1}{2} \bar{\mathbf{u}}^2 + \tilde{\mathbf{u}} \cdot \bar{\mathbf{u}} \right) - (\tilde{\mathbf{u}} + \bar{\mathbf{u}}) \times \boldsymbol{\omega}$ . Time averaging of the latter expression yields  $\langle (\mathbf{u} \cdot \nabla) \mathbf{u} \rangle = \nabla \langle \frac{1}{2} \tilde{u}^2 \rangle + (\bar{\mathbf{u}} \cdot \nabla) \bar{\mathbf{u}}$ . Likewise, time averaging of (3.29) leads to

$$\partial_t \bar{\mathbf{u}} + (\bar{\mathbf{u}} \cdot \nabla) \bar{\mathbf{u}} = -\frac{1}{\rho} \nabla \left( \bar{p} + \rho g z + \frac{1}{2} \rho \langle \tilde{u}^2 \rangle \right) + \nu \nabla^2 \bar{\mathbf{u}}. \quad (3.30)$$

By defining  $p' \equiv \bar{p} + \rho g z + \frac{1}{2} \rho \langle \tilde{u}^2 \rangle$ , the equation for the evolution of the steady part of  $\mathbf{u}$  becomes identical to a Navier-Stokes equation with no external forcing. It can also be shown that the incompressibility condition for the steady field remains unchanged so  $\nabla \cdot \bar{\mathbf{u}} = 0$ . The boundary conditions to solve the system are those provided in the junction between the boundary layers and the bulk found in §3.1, *e.g.* (3.27). This will be referred to as the matched boundary condition. Thus, the streaming flow generated in the bulk can be computed by solving classic Navier-Stokes equations with non-trivial boundary conditions.

Remarkably, the contribution due to the local oscillatory velocity field only appears in the effective pressure in (3.30) and has null effect on  $\bar{\mathbf{u}}$  at leading order. The steady component of the flow stemming from the nonlinearities in the bulk is thus negligible in comparison with the streaming generated by the boundary layer. Henceforth, we expect that the boundary layers are the main responsible for the appearance of streaming in quasi-inviscid stationary waves.

### 3.3. Classical Faraday waves

#### 3.3.1. General case

Here, we apply our previous findings to the classical Faraday waves. The container is assumed to be a rectangular impermeable tank of horizontal dimensions  $L_x, L_y$  filled up to height  $h$ . The fluid then occupies the domain  $(x, y, z) \in [0, L_x] \times [0, L_y] \times [-h, 0]$  as shown in figure 5(b).

In the limit of ideal flows, the instantaneous fields in Faraday waves are modelled by a velocity potential  $\Phi$  inside the bulk,

$$\Phi(x, y, z, t) = A \cos(k_1 x) \cos(k_2 y) \frac{\cosh(k(z+h))}{\cosh(kh)} \cos(\omega t), \quad (3.31)$$

where  $k_1$  and  $k_2$  are multiples of  $\pi/L_x$  and  $\pi/L_y$  respectively, and  $k = \sqrt{k_1^2 + k_2^2}$ .  $\mathbf{U}_0$  is related to  $\Phi$  through  $\mathbf{U}_0 = \nabla \Phi$ . Hence, the oscillatory tangential velocity field at the boundaries can be evaluated via equation (3.31) and then plugged into equation (3.27) to obtain the matched boundary condition for the streaming field. These streaming boundary conditions will then be used in §4 to compute the streaming in the bulk through equation (3.30).

*Vertical walls:*

At  $x = \{0, L_x\}$ , the tangential velocity field is

$$\begin{aligned} \underline{u}_0 &= 0, \\ (\underline{v}_0, \underline{w}_0) &= \pm A \cos(\omega t) \left( -k_2 \sin(k_2 y) \frac{\cosh k(z+h)}{\cosh kh}, k \cos(k_2 y) \frac{\sinh k(z+h)}{\cosh kh} \right), \end{aligned} \quad (3.32)$$

which is used to get the matched streaming boundary conditions by applying (3.27)

$$\begin{aligned} \langle \underline{u}_1 \rangle &= 0, \\ (\langle \underline{v}_1 \rangle, \langle \underline{w}_1 \rangle) &= \frac{A^2}{8\omega C_0^2} (k_2 \sin(2k_2 y) [3k_1^2 C_z^2 - k^2], -k S_{2z} [3k_1^2 \cos^2(k_2 y) + k_2^2]). \end{aligned} \quad (3.33)$$

Here we have compacted the notations  $\cosh(k(z+h))$ ,  $\sinh(k(z+h))$  and  $\sinh(2k(z+h))$  into  $C_z$ ,  $S_z$  and  $S_{2z}$ , respectively ( $C_0$  stands for  $\cosh(kh)$ ). By permuting the coordinates  $x \leftrightarrow y$ , components  $u \leftrightarrow v$  and indices  $1 \leftrightarrow 2$ , we deduce the matched streaming boundary conditions at the two other walls  $y = \{0, L_y\}$ .

$$\begin{aligned} (\langle \underline{u}_1 \rangle, \langle \underline{v}_1 \rangle) &= \frac{A^2}{8\omega C_0^2} (k_1 \sin(2k_1 x) [3k_2^2 C_z^2 - k^2], -k S_{2z} [3k_2^2 \cos^2(k_1 x) + k_1^2]), \\ \langle \underline{v}_1 \rangle &= 0. \end{aligned} \quad (3.34)$$

*Bottom:*

The bottom of the tank corresponds to  $z = -h$ . The instantaneous velocity fields read there

$$(\underline{u}_0, \underline{v}_0) = -A \cos(\omega t) \left( k_1 \frac{\sin(k_1 x) \cos(k_2 y)}{\cosh kh}, k_2 \frac{\cos(k_1 x) \sin(k_2 y)}{\cosh kh} \right) \quad (3.35)$$

and the resulting matched boundary conditions are

$$\begin{aligned} (\langle \underline{u}_1 \rangle, \langle \underline{v}_1 \rangle) &= -\frac{A^2}{8\omega C_0^2} (k_1 \sin(2k_1 x) [3k^2 \cos^2(k_2 y) - k_2^2], k_2 \sin(2k_2 y) [3k^2 \cos^2(k_1 x) - k_1^2]), \\ \langle \underline{w}_1 \rangle &= 0. \end{aligned} \quad (3.36)$$

*Top interface:*

At the interface ( $z = 0$ ), we have chosen two types of boundary conditions that can be applied to the streaming field. The first one is

$$\begin{aligned} \partial_z \langle \underline{u}_1 \rangle &= \partial_z \langle \underline{v}_1 \rangle = 0, \\ \langle \underline{w}_1 \rangle &= 0, \end{aligned} \quad (3.37)$$

for uncontaminated surfaces. This condition is equivalent to the classic free-surface condition, i.e. null tangential stress at  $z = 0$  (Batchelor, G. K. 2000). The second one is

$$\begin{aligned} \langle \underline{w}_1 \rangle &= 0, \\ (\langle \underline{u}_1 \rangle, \langle \underline{v}_1 \rangle) &= -\frac{A^2}{8\omega} (k_1 \sin(2k_1 x) [3k^2 \cos^2(k_2 y) - k_2^2], k_2 \sin(2k_2 y) [3k^2 \cos^2(k_1 x) - k_1^2]), \end{aligned} \quad (3.38)$$

for fully contaminated surfaces. This condition is due to the presence of an inextensible film at the surface (Miles 1967; Henderson & Miles 1994; Martin & Vega 2005).

### 3.3.2. Case of longitudinal waves: $k_2 = 0$

We now focus on the case of plane stationary waves characterised by  $k_2 = 0$ , which corresponds to the striped Faraday-waves patterns that can easily be observed in containers whose transverse dimension is much smaller than the critical wavelength. Waves in this case are almost two-dimensional. Nevertheless, some three-dimensional effects may still

---

	$\langle u_1 \rangle$	$\langle v_1 \rangle$	$\langle w_1 \rangle$
Bottom: $z = -h$	$-\frac{3}{8} \frac{A^2 k^3}{\omega C_0^2} \sin(2kx)$	0	0
Lateral walls: $x = \{0, L_x\}$	0	0	$-\frac{3}{8} \frac{A^2 k^3}{\omega C_0^2} \sinh(2k(z+h))$
Front walls: $y = \{0, L_y\}$	$-\frac{1}{8} \frac{A^2 k^3}{\omega C_0^2} \sin(2kx)$	0	$-\frac{1}{8} \frac{A^2 k^3}{\omega C_0^2} \sinh(2k(z+h))$
Top interface: $z = 0^*$	$-\frac{3}{8} \frac{A^2 k^3}{\omega} \sin(2kx)$	0	0
$z = 0^\dagger$	$\partial_z \langle u_1 \rangle = 0$	$\partial_z \langle v_1 \rangle = 0$	0

---

TABLE 2. Streaming matched boundary conditions for longitudinal Faraday waves ( $k = k_1, k_2 = 0$ ). Only the conditions at the top interface change for a fully contaminated interface (\*) and an uncontaminated one ( $\dagger$ ). These boundary conditions are used in the numerical simulations presented in §4.

---

be present due to the presence of the walls in the transverse direction, which induces alteration of the streaming flow through its viscosity. The expression for the instantaneous potential  $\Phi$  is thus changed to

$$\Phi(x, y, z, t) = A \cos(kx) \frac{\cosh k(z+h)}{\cosh kh} \cos(\omega t), \quad (3.39)$$

where naturally  $k_1 = k$ . As a result, the matched boundary conditions for the streaming velocities are also simplified. The results are summarised in table 2.

### 3.3.3. Two-dimensional flow

When the problem is completely homogeneous in the  $y$  direction (absence of transverse walls,  $\partial_y = 0, v = \langle v_1 \rangle = 0$ ), the potential takes the same expression as in the case  $k_2 = 0$  (3.39). The matched boundary conditions in table 2 remain similar while those at the transverse walls drop. The transverse walls are the only source of differences between the  $k_2 = 0$  and the two-dimensional flow. In the former case, the presence of the wall is expected to induce a three-dimensional streaming field.

## 4. Numerical simulations

In order to solve equations (3.30) with the matched boundary conditions from table 2 provided by the theory, we require numerical simulations. They allow us to address two basic questions: Can we reproduce experimental observations using the boundary-layer-induced streaming theory? Is it sufficient to keep a two-dimensional approximation or do three-dimensional effects play an important role?

### 4.1. Numerical methods

To run simulations of the streaming flow inside the incompressible vibrating fluid, we implemented our own code. The code directly integrates the Navier-Stokes equations with the divergence-free condition (3.30) in a parallelepiped domain delimited at the top by the interface of the fluid at rest (see figure 5(b)). The flat top interface is a fair approximation for the time-averaged position of low amplitude Faraday waves. In (3.2), the gravity and the vertical vibration are gathered with the pressure to form a time-dependent effective pressure and do not have any effect on the velocity fields since a single fluid of constant density is involved in this model. In the code, the fields are discretised by finite-difference schemes using the MAC (Marker And Cell) disposition on a regular staggered mesh

where the pressure is computed at the centre of each cell and the components of the velocity are located at the faces corresponding to their direction. The incompressible Navier-Stokes equations are solved by a projection method (Chorin 1968). The pressure is computed incrementally with a BiCGStab (Stabilised BiConjugate Gradient) method. The spatial discretisation is made with standard centred schemes of second order except the advection terms for which ENO (Essentially Non Oscillatory) schemes are used. The temporal stepping involves a first-order forward Euler discretisation with adaptive time steps to ensure numerical stability.

The simulations use the equations from table 2 as matched boundary conditions, with the three quantities,  $k$ ,  $\omega$  and  $A$ , fixed. We recall that for longitudinal waves the wave number is defined as  $k = m\pi/L_x$  with  $m$  an integer, and  $\omega$  is deduced from  $k$  by means of (2.1) in consistency with the experiments. At dominant order, the amplitude  $A$  is related with the amplitude of Faraday waves  $\Delta\zeta = \max_{x,t}(\zeta) - \min_{x,t}(\zeta)$  by

$$A \sim \frac{g\Delta\zeta}{\omega}. \quad (4.1)$$

We emphasize some features about the theoretical model and the simulations. First, the fact that the coefficients  $k$ ,  $\omega$  and  $A$  are set up manually renders the model and the simulations independent of the bifurcation criticality, a feature consistent with the experimental results. Second, all the matched boundary conditions for the streaming flow are proportional to  $A^2/\omega$ . Hence, cases with altered  $\omega$  are also swept by varying  $A$ ; the complete model could be rewritten as a function of the single variable  $A' = A/\sqrt{\omega}$  instead of  $\omega$  and  $A$  separately, reducing the dimension of the parameter space.

#### 4.2. Numerical results

In this section, most of the parameters of interest are the same as in the experiment: the density  $\rho = 1.1 \text{ g/cm}^3$ , the dynamic viscosity  $\nu = 9.09 \times 10^{-3} \text{ cm}^2/\text{s}$ , the dimensions of the fluid layer  $L_x \times L_y \times h = (19.05 \times 2.54 \times 2) \text{ cm}^3$  and the number of nodes in the longitudinal direction  $m = 4, 5, 6, 7$ . The corresponding frequencies of Faraday waves given by the dispersion relation (2.1) are  $f/2 = 3.8 \text{ Hz}, 4.45 \text{ Hz}, 4.95 \text{ Hz}$  and  $5.4 \text{ Hz}$ , respectively (the frequency of vibration of the container corresponds to  $f$  as shown in table 1). The amplitude  $A$  is varied between  $0.4 \text{ cm}^2/\text{s}$  and  $1.26 \times 10^2 \text{ cm}^2/\text{s}$ , where the lowest bound is the value below which the streaming flow remains qualitatively unchanged and the upper bound is the value at which the code diverges. The regular discretised mesh contains  $240 \times 80 \times 80$  cells. Simulations are performed with both the uncontaminated and the fully contaminated boundary conditions at the interface, cf. table 2. In figures 6–7, we first show the instantaneous streamlines and associated velocity field of the streaming flow in the  $y$  midplane. We set  $m = 7$ ,  $f/2 = 5.4 \text{ Hz}$  on an uncontaminated interface as  $A$  is varied.

Likewise, in figures 8–9, we plot respectively the instantaneous streamlines and the associated velocity fields of the Faraday streaming flow for the same values of  $m$  and  $\omega$  but for the fully contaminated case.

Comparison of figures 6–7 with 8–9 show that contamination induces very unlike streaming flows at low amplitudes. The low-amplitude fully contaminated Faraday streaming flows are very similar to the type-I patterns found in the experiments, with weakly spiraling loops at the top of the domain and small recirculations at the bottom. The fact that the streaming flows do not form perfectly closed loops is related to the presence of transverse variations of the velocity component  $v$ . The features of the flow are then expected to differ from those obtained with the two-dimensional theory, even on the  $y$  midplane. The experimental patterns of type I (figures 2–3, patterns (c) and (d)) display

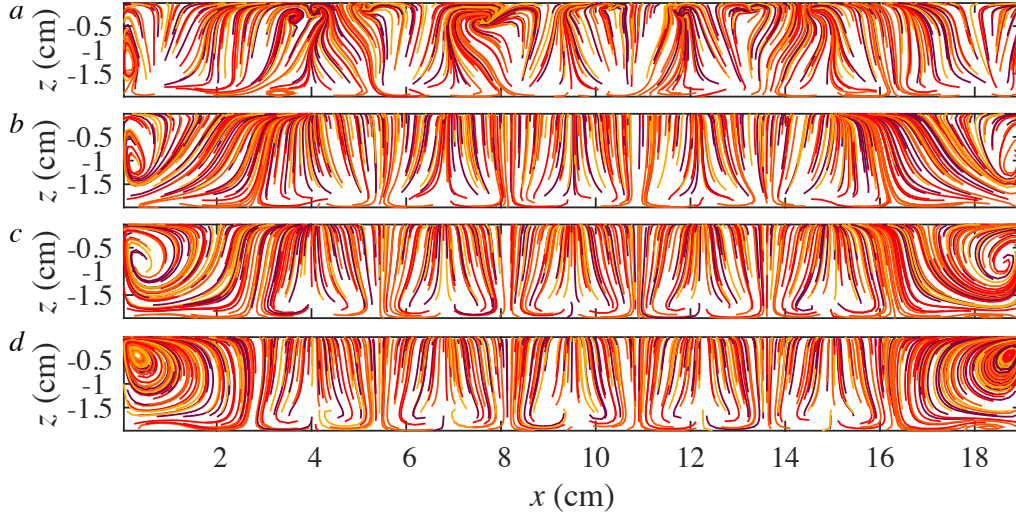


FIGURE 6. Instantaneous streamlines in the  $y$  midplane for  $m = 7$  and varying  $A$  with uncontaminated interface. The amplitude  $A$  increases from the bottom to the top: (a) 71.1, (b) 40, (c) 22.5 and (d)  $0.4 \text{ cm}^2/\text{s}$ .

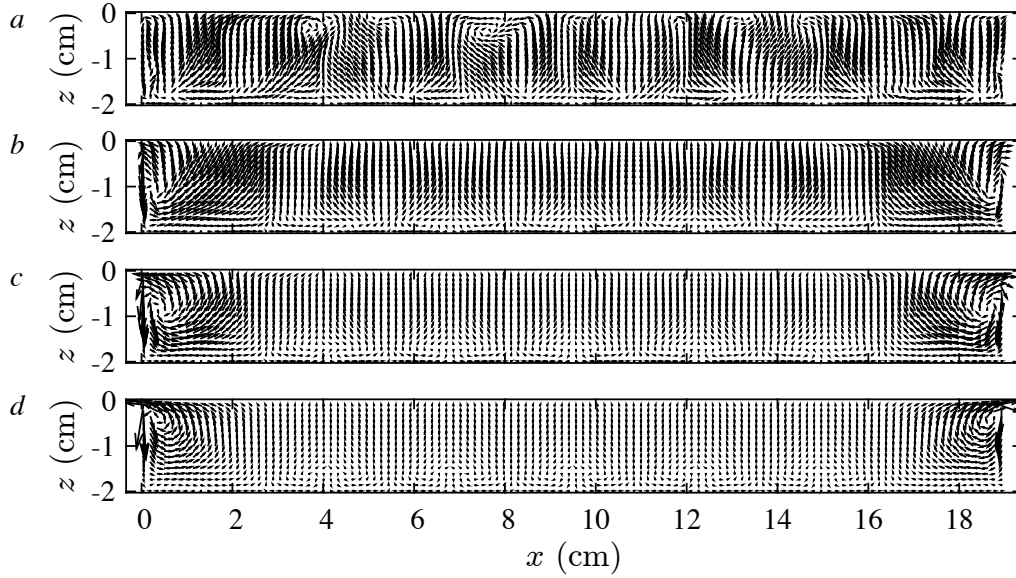


FIGURE 7. Instantaneous velocity field in the  $y$  midplane for  $m = 7$  and varying  $A$  with uncontaminated interface. Amplitudes are the same as in figure 6.

the strongest similarities with the simulated fields of figures 8–9 at moderate amplitude  $A = 22.5 \text{ cm}^2/\text{s}$ . Therein, both the streamlines and the velocity fields have very similar shapes.

The uncontaminated Faraday streaming flows look completely different from the fully contaminated ones and contrast with all the patterns observed in the experiments. However, they display similarities with the type-II patterns, namely the presence of accumulation points at the vicinity of the interface, suggesting again that the flow is fairly three-dimensional on the  $y$  midplane. In contrast, there are no loops at the top of the



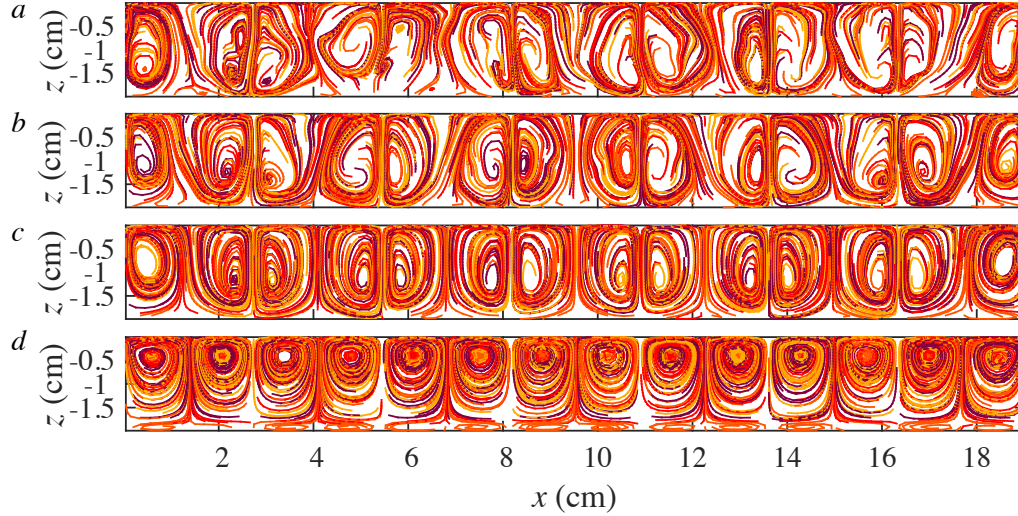


FIGURE 8. Instantaneous streamlines in the  $y$  midplane for  $m = 7$  and varying  $A$  with fully contaminated interface. Same amplitudes as in figure 6.

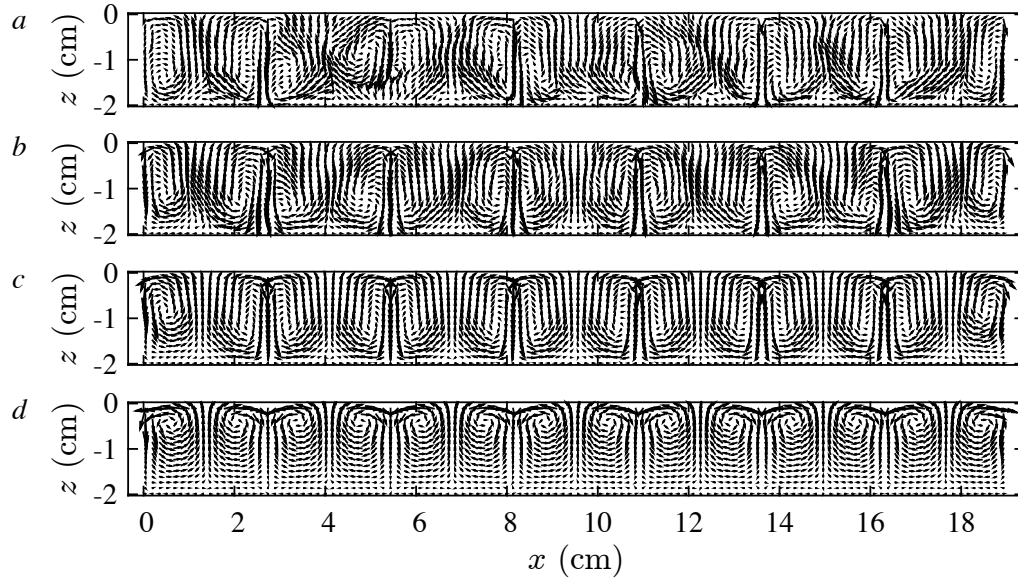


FIGURE 9. Instantaneous velocity field in the  $y$  midplane for  $m = 7$  and varying  $A$  with fully contaminated interface. Same amplitudes as in figure 6.

domain. Intermediate contamination, or in other words matched boundary conditions between (3.37) and (3.38) as in (Martin *et al.* 2002), might improve the resemblance between experiments and simulations.

Examples of disordered Faraday streaming flows are shown at larger amplitudes like  $A = 71.1 \text{ cm}^2/\text{s}$  at the top of each figure 6–9. When disorder comes, streaming flows become unsteady as well. The emergence of disorder generally occurs at values of  $A$  of that order of magnitude, regardless the interface contamination and for all the wave numbers explored in this work.

Varying the wave number  $m$  in the matched boundary conditions does not have any



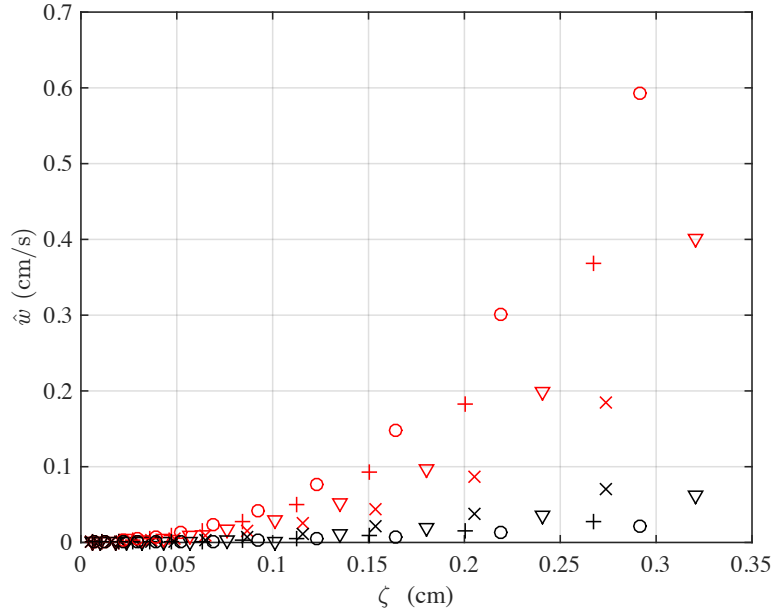


FIGURE 10. Bifurcation diagram for simulations of streaming patterns. Red signs represent contaminated Faraday streaming flows, which share most properties of the Type-I patterns. Black signs stand for uncontaminated Faraday streaming flows that are roughly similar to type-II patterns. The markers  $\times$ ,  $\nabla$ ,  $+$  and  $\circ$  correspond to  $m=4, 5, 6$  and  $7$ , respectively.

dramatic effect in the flow structure. Besides the expected change of wavelength of the streaming flows that occurs, one can notice the loops at the walls are overcome by the central patterns as  $m$  is decreased, particularly in the uncontaminated case.

We then focus on more quantitative aspects of the Faraday streaming flows to compare our simulations with the experimental results presented in figure 4. Taking the same definition of the average velocity  $\hat{w}$  as in §2.4, we plot in figure 10 a comparable bifurcation diagram. Different symbols correspond to different  $m$  values (see caption), while different colours distinguish between patterns obtained with contaminated surface (in red) from those obtained with uncontaminated surface (in black). We recall that uncontaminated patterns share some properties with type-II patterns, while contaminated ones resemble type-I patterns.

Figures 4 and 10 show remarkable similarities. First,  $\hat{w}$  increases faster than linearly in  $\zeta$ . In the two cases,  $\hat{w}$  displays small values for  $\zeta < 0.15$  cm. We also observe fair agreement as the uncontaminated Faraday streaming flows generate lower vertically averaged velocities than contaminated Faraday streaming flows. Finally The values of  $\hat{w}$  obtained in simulations are remarkably close to those measured in the experiments. However, there is an important discrepancy between the numerical simulation and the experiments: simulations do not show a collapse of the branches as the experiments, but instead, scattered branches with an important dependence on  $m$ . The origin of this disagreement is still an open issue. It may come from unsufficiently controled surface properties in the experiment, or from the absense of noise in simulations.

To see whether the two-dimensional approximation used in previous works is good enough to explain qualitatively the streaming field, we exploit the tridimensional data obtained from the numerical simulations. First, we compare the three-dimensional streaming patterns of our numerical simulations in the  $y$  midplane (figures 6–9) to their two-

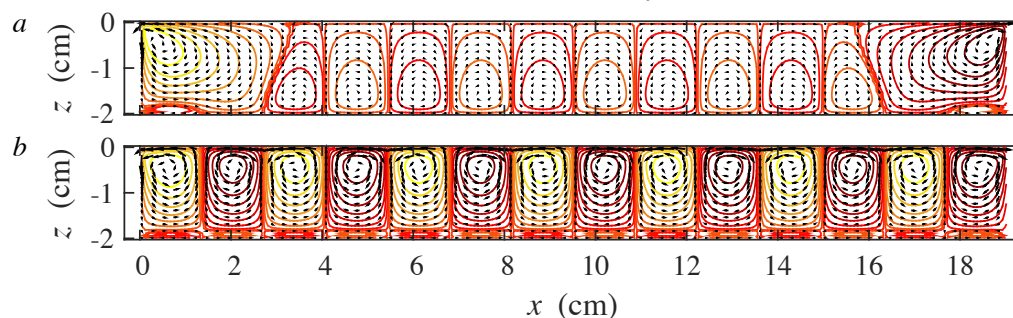


FIGURE 11. Velocity fields (arrows) and streamlines (contours) of the two-dimensional streaming flow for  $m = 7$  and  $A = 0.4 \text{ cm}^2/\text{s}$ . From top to bottom: (a) with uncontaminated interface and (b) with fully contaminated interface.

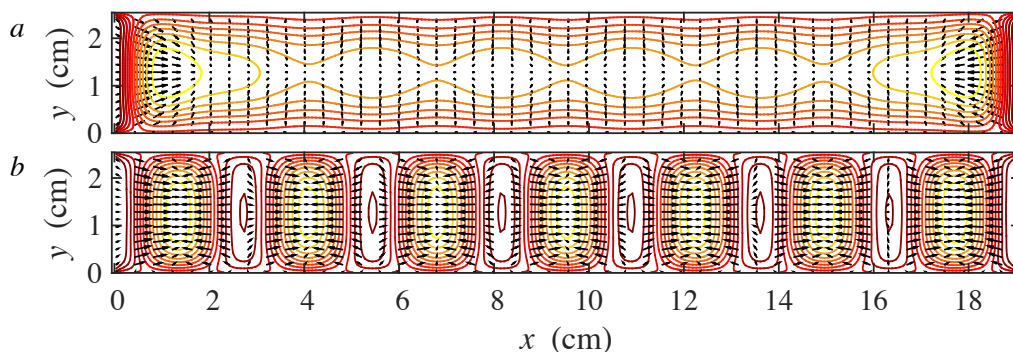


FIGURE 12. Velocities of the streaming flow in the horizontal plane  $z = -1 \text{ cm}$  for  $m = 7$  and  $A = 0.4 \text{ cm}^2/\text{s}$ . Arrows represent the horizontal velocity components  $(u, v)$  while contours stand for  $w$ . From top to bottom: (a) with uncontaminated interface and (b) with fully contaminated interface.

dimensional counterparts (figure 11) at low amplitude  $A = 0.4 \text{ cm}^2/\text{s}$  and for  $m = 7$ . For this purpose, we ran a two-dimensional simplified version of the code following §3.3.3. The main qualitative differences between the streaming fields of figures 6–9 and the two-dimensional ones of figure 11 stem from the fact that streamlines become perfectly closed loops when the flow is purely two-dimensional, as expected. The differences are localized far from the walls of the domain and are especially striking in the uncontaminated case (compare figure 11 (a) with figures 6 (d) and 7 (d)). The differences remain visible when the interface is contaminated at the frontier between two superposed loops, but in a lesser extent (compare figure 11 (b) with figures 8 (d) and 9 (d)). Nevertheless, the main differences between the two dimensional streaming flows and the three-dimensional ones are located in regions where the streaming velocity is weak.

Transverse effects are more visible in horizontal planes, for instance at  $z = -1 \text{ cm}$  as shown in figure 12. They are highlighted by significant gradients of  $w$  in the transverse direction. Likewise, perceptible deviations of the velocity from or towards the midplane  $y = L_y/2$  are observed. The transverse effects are more marked near the walls and exacerbate with increasing wave amplitude  $A$  and decreasing trough width  $L_y$ . These assessments indicate that three-dimensional effects on Faraday streaming flows are noticeable, even for longitudinal waves. This contrasts with the weak and local effect of walls on Faraday surface waves.

Finally, we depict the motion of fluid particles inside the bulk in the low amplitude

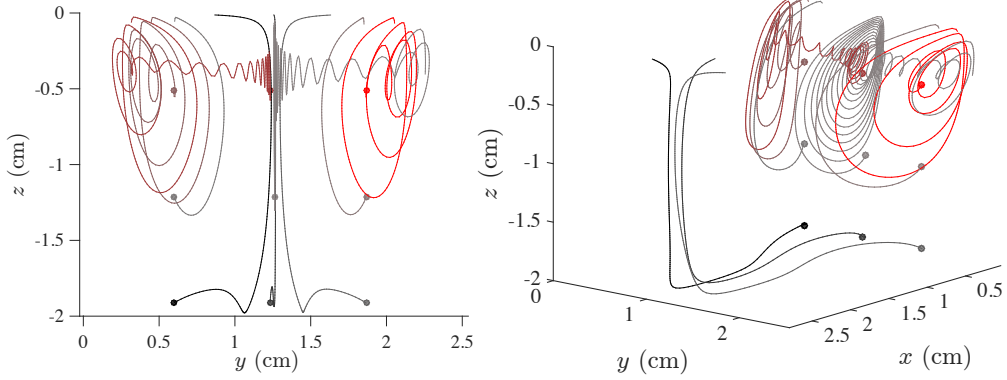


FIGURE 13. Trajectories of particles starting from various points of the plane  $x = 0.28$  cm (first cell) for  $m = 7$ ,  $f/2 = 5.4$  Hz and  $A = 0.4$  cm<sup>2</sup>/s with uncontaminated interface. Left: viewed from the face  $x = 0$ . Right: slanted view. Each color denotes the trajectory of the same particle in left and right plots. The starting points of the paths are represented by disks.

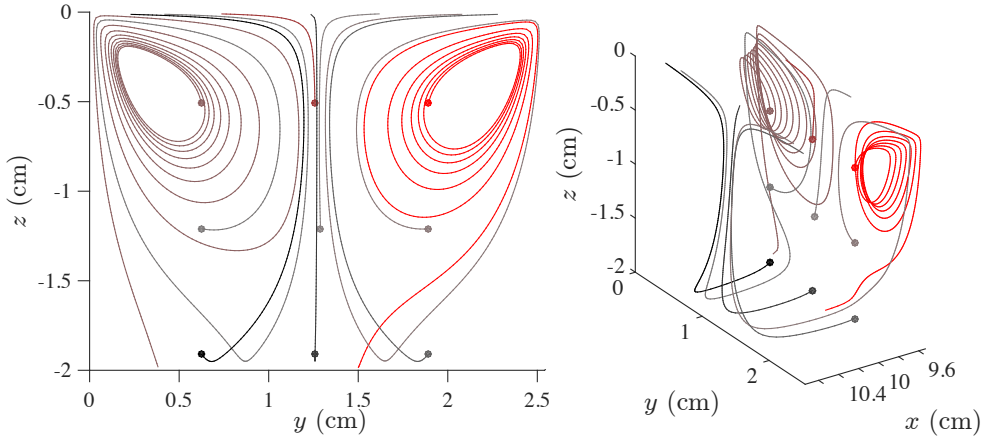


FIGURE 14. Trajectories of particles starting from various points of the plane  $x = 9.80$  cm (central cell) for  $m = 7$ ,  $f/2 = 5.4$  Hz and  $A = 0.4$  cm<sup>2</sup>/s with uncontaminated interface. Left: viewed from the face  $x = 0$ . Right: slanted view. Each color denotes the trajectory of the same particle in left and right plots. The starting points of the paths are represented by disks.

limit, by plotting streamlines outside the  $y$  midplane. We restrict ourselves to the lowest amplitude of patterns  $A = 0.4$  cm<sup>2</sup>/s where the approximations necessary for the theory of streaming are largely satisfied. Figures 13–14 represent the trajectories of particles in the uncontaminated case for two longitudinal planes,  $x = 0.28$  cm and  $x = 9.8$  cm (respectively close to a side wall and close to the  $x$  mid plane). We show the same data for the fully contaminated interface in figures 15–16.

In all the figures 13–16, the  $y$  midplane, which is a symmetry plane of the problem, plays the role of separatrix between both halves of the domain: particles starting within a half stay indefinitely there. The  $x$  midplane plays the same role of separatrix. A more detailed inspection shows that all the planes of equation  $x = m' L_x / (2m)$  are separatrices too,  $m'$  being an integer, except those at  $m' = 1$  and  $m' = m - 1$  in the uncontaminated case (compare the span of the trajectories in the  $x$  direction in figure 13 and 14–16). Hence, the motion of a fluid particle remains confined to small portions of the box of length  $L_x / (2m)$  and width  $L_y / 2$ , depending on its starting point. The separatrices are

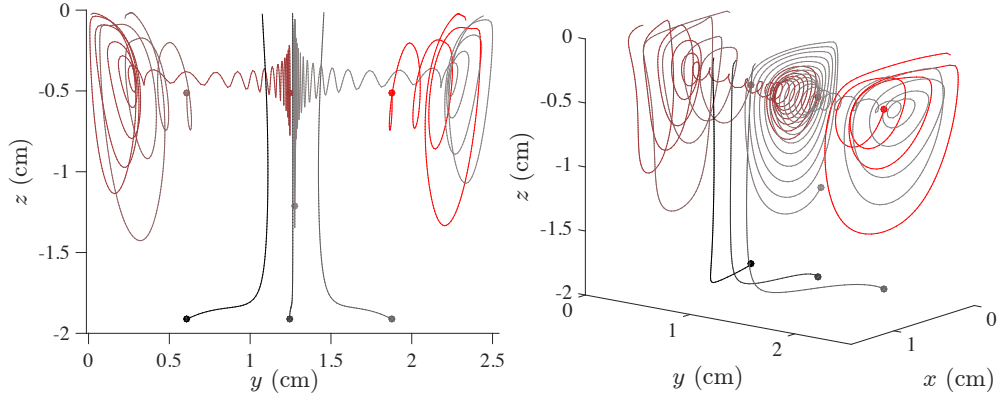


FIGURE 15. Trajectories of particles starting from various points of the plane  $x = 0.28$  cm (first cell) for  $m = 7$ ,  $f/2 = 5.4$  Hz and  $A = 0.4 \text{ cm}^2/\text{s}$  with fully contaminated interface. Left: viewed from the face  $x = 0$ . Right: slanted view. Each color denotes the trajectory of the same particle in left and right plots. The starting points of the paths are represented by disks.

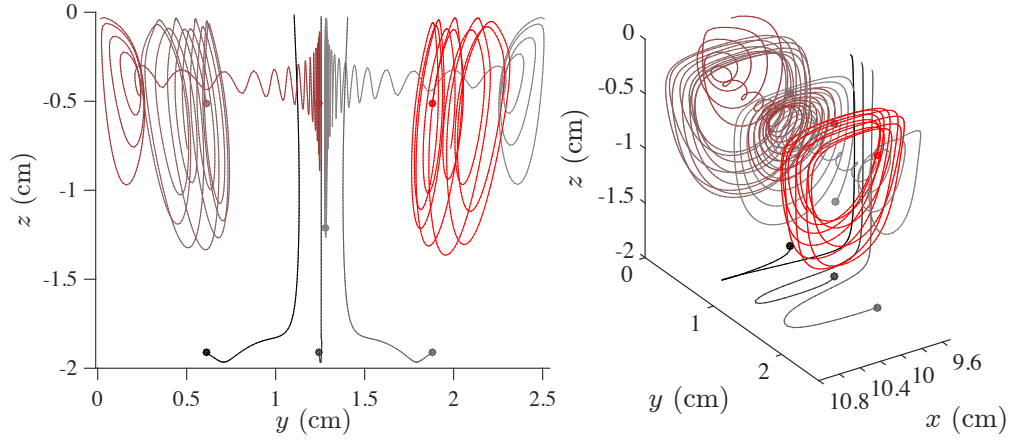


FIGURE 16. Trajectories of particles starting from various points of the plane  $x = 9.80$  cm (central cell) for  $m = 7$ ,  $f/2 = 5.4$  Hz and  $A = 0.4 \text{ cm}^2/\text{s}$  with fully contaminated interface. Left: viewed from the face  $x = 0$ . Right: slanted view. Each color denotes the trajectory of the same particle in left and right plots. The starting points of the paths are represented by disks.

also visible in figures 6–8 at the locations of vertical streamlines as well as in figure 12 separated by the orthogonal planes of null  $u$  or  $v$  components. It is important to emphasize that odd  $m'$  values correspond to nodes of the interface vibration whereas even  $m'$  values, to the antinodes.

Outside the separatrices, the complexity of the trajectories is mainly illustrated by the paths on the upper part of the domain. The loops formed by the trajectories differ in figure 14, displaying orthogonal directions to those of figures 13, 15 and 16. In this case, the motion displays a transverse components stronger than the longitudinal one. This is due to the absence of constraints on the velocity field at the top (Neumann conditions) and the distance to the lateral boundaries. The separatrices disappear when the amplitude increases and the patterns become disordered. The trajectories of all fluid particles span to the whole domain.

## 5. Summary and discussion

In this work, we have studied the steady streaming flows sustained by longitudinal Faraday waves in a rectangular container. We have faced this problem by performing experiments, developing a theoretical framework and running numerical simulations.

In the experiments conducted in §2 we report the observation of streaming flows with a well-resolved spatial structure. These patterns appear at any wavenumber, but their morphology may vary among three types. Type I corresponds to well-defined counter-rotative rolls, Type II, to moustache-like patterns and Type III, to irregular patterns. All these patterns have been observed when performing stroboscopic measurements of tracers, which naturally filters off the periodic motion of standing surface waves. We have obtained the flow streamlines by superposing the sequence of images, and the flow velocity field by performing PIV analysis. Results were summarized in a bifurcation diagram for the streaming vertical velocity as a function of the wave amplitude (figure 4). All the data collapses into two branches distinguishing type-I patterns from type-II and type-III ones. Furthermore, the type-I and II branches coexist in a common range of forcing parameters, which means that identical Faraday waves can sustain qualitatively different streaming flows. Other parameters, such as the wavelength or the bifurcation criticality do not show any important qualitative role.

We developed a theory for the streaming due to oscillatory flows in §3, extending the results of Batchelor to three dimensional configurations. The theory is based on boundary layers generated by tangential oscillating flows in the vicinity of rigid walls. We show that boundary layers slowly induce a vorticity into the bulk until a steady state—the streaming flow—is reached. Starting from Navier-Stokes equations, we split the fluid domain in two regions: the bulk, where viscosity is neglected, and the boundary layer where viscosity plays a major role. Then, using asymptotic analysis, we find the right hierarchy of equations which allows us to match the bulk and the boundary layer flows at the junction. At this point we introduced a flow solution having both an oscillatory and a steady component. By performing time averages along a period of oscillation, we extract the steady component of the flow in the boundary layer. Equations show that the streaming inside the boundary layer induces a net streaming in the junction with the bulk, which can then be used as a matched boundary condition for the bulk region. In the two-dimensional case, these conditions are consistent with those obtained by Batchelor, G. K. (2000). Finally, the theory explains that the boundary layers represent the main source of streaming in the vibrating fluid layer, (corrections due to nonlinearities in the bulk are of higher order). Focused on our experiments, we have applied this general theory to find the streaming induced by the rigid-walls in longitudinal Faraday waves in a rectangular container. On the other hand, complementary boundary conditions at the free surface have been fixed accounting for clean and fully contaminated cases.

Using the theoretical results, we performed direct numerical simulations aiming to the steady component sustained by Faraday waves. This has been applied to a rectangular domain with a single fluid, where the oscillating Faraday wave main flow only couple through the matched boundary conditions previously deduced. From the simulations we have observed various types of streaming patterns, depending on the surface conditions. In the case of fully contaminated surface, we have obtained counter-rotative structures that strikingly resemble type-I patterns observed in our experiments. For a clean surface, similarities with experiments have also been found although in a less conclusive way. Considering conditions of intermediate contamination (Martin & Vega 2005) may improve the agreement with patterns of type-II. Irregular patterns (type III) have been observed in simulations when the forcing amplitude is increased for any surface condition.

Then we have computed a bifurcation diagram analogous to the experimental one. We have observed that quantitatively, results obtained in simulations are compatible with experimental measurements. Also, our results with a contaminated surface and clean surface present distinguishable vertical velocities. However, the collapse of the curves found in experiments is not observed in the numerical results, an issue which deserves further investigation. Then we have focussed on whether the transversal effects are truly negligible. The comparison between three-dimensional streaming flows and two-dimensional ones shows that the walls in the third dimension have an important effect on the streaming flow, remarkably large compared to their effect on surface waves. By computing the horizontal components of the velocity fields and the trajectories of several fluid particles, we have concluded that a two-dimensional approximation is not enough to catch the richness of the flow beneath Faraday waves.

The original investigation of Faraday (1831) and recent experimental attempts (Falkovich *et al.* 2005; Sanli *et al.* 2014) have naturally risen the question about how streaming flows may influence the motion of floaters or heavy particles. Despite it is out of the scope of the present investigation, our results show that streaming flows are another mechanism leading to slow time scale motion of such particles. Contrary to weight and buoyancy that can only induce vertical motion, the average drag induced by the streaming does contribute with horizontal net forces exerted on the particles, even when they are constrained to the bottom or top of the fluid. In particular, the discussed set of separatrices act as basins of repulsion and attraction for particles, whose locations depend on both the wavelength of the Faraday waves and the contamination of the surface. This interesting perspective will be the subject of a rich field for further exploration.

Finally, the comparison between numerical and experimental results presented in this work poses an interesting issue. While the numerical results point to the free surface contamination as the only variable dramatically affecting the streaming flow, the experimental results show that identical Faraday waves (same fluid under same conditions) may mask qualitatively different streaming flows. The link will strikingly require that the same liquid can display different contamination degrees, which is contrastable with the general assumption in the literature that the degree of contamination is a static feature of the flow. This provides a hint that contaminants are not just passively dragged by the streaming flow but also exert a feedback on it: a feature which enriches the streaming problem even further.

## Acknowledgements

We are grateful to Héctor Alarcón for fruitful discussions. LG was supported by Conicyt/Becas Chile de Postdoctorado 74150032. PG was supported by Conicyt/Fondecyt Postdoctorado 3140550. NP was supported by Conicyt/Fondecyt Postdoctorado 3140522. HU was supported by Fondecyt 11130450. The laser, the fast camera and some other parts of the setup were purchased under the funding program Conicyt AIC-43. Powered@NLHPC: This research was partially supported by the supercomputing infrastructure of the NLHPC (ECM-02).

## REFERENCES

- BATCHELOR, G. K. 2000 *An Introduction to Fluid Dynamics*. Cambridge, UK: Cambridge University Press.
- BENDER, C. M. & ORSZAG, S. A. 1999 *Advanced Mathematical Methods for Scientists and Engineers: Asymptotic Methods and Perturbation Theory*. New York, US: Springer-Verlag.



- CHEN, PU, LUO, ZHENGYUAN, GÜVEN, SINAN, TASOGLU, SAVAS, GANESAN, ADARSH VENKATARAMAN, WENG, ANDREW & DEMIRCI, UTKAN 2014 Microscale Assembly Directed by Liquid-Based Template. *Adv. Mater.* **26** (34), 5936–5941.
- CHLADNI, E.F.F. 1787 *Entdeckungen über die Theorie des Klängen*. Wittenberg.
- CHORIN, A J 1968 Numerical solution of the Navier-Stokes equations. *Mathematics of computation* .
- COLES, D 1965 Transition in circular Couette flow. *J. Fluids Mech.* **21**, 385–425.
- DOUADY, S. 1990 Experimental study of the Faraday instability. *J. Fluids Mech.* **221**, 383–409.
- FALKOVICH, G, WEINBERG, A, DENISSENKO, P & LUKASCHUK, S 2005 Surface tension: Floater clustering in a standing wave. *Nature* **435** (7045), 1045–1046.
- FARADAY, M. 1831 On a peculiar class of acoustical figures; and on certain forms assumed by groups of particles upon vibrating elastic surfaces. *Philos. T. Roy. Soc. A* **121**, 299–340.
- GORDILLO, L 2012 Non-Propagating Hydrodynamic Solitons in a Quasi-One-Dimensional Free Surface Subject to Vertical Vibrations. PhD thesis, Universidad de Chile, Santiago.
- GORDILLO, L & MUJICA, N. 2014 Measurement of the velocity field in parametrically excited solitary waves. *J. Fluids Mech.* **754**, 590–604.
- GUTIÉRREZ, P. & AUMAÎTRE, S. 2016 Clustering of floaters on the free surface of a turbulent flow: an experimental study. Submitted.
- HENDERSON, D. & MILES, J. W. 1994 Surface wave damping in a circular cylinder with a fixed contact line. *J. Fluids Mech.* **275**, 285–299.
- LAMB, H. 2006 *Hydrodynamics*, 6th edn. Cambridge, UK: Cambridge University Press.
- LIDE, D. R. 2004 *Handbook of Chemistry and Physics*, 85th edn. Boca Raton, US: Chemical Rubber Company Press.
- LONGUET-HIGGINS, M S 1953 Mass Transport in Water Waves. *Philos. T. Roy. Soc. A* **245**, 535.
- MARTIN, E, MARTEL, C. & VEGA, J. M 2002 Drift instability of standing Faraday waves. *J. Fluids Mech.* **467**, 57–79.
- MARTIN, E & VEGA, J. M 2005 The effect of surface contamination on the drift instability of standing Faraday waves. *J. Fluids Mech.* **546**, 203–225.
- MEINHART, C. D., WERELEY, S. T. & SANTIAGO, J. G. 2000 A PIV algorithm for estimating time-averaged velocity fields. *J. Fluids Eng.* **122** (2), 285–289.
- MILES, J. W. 1967 Surface-Wave Damping in Closed Basins. *Proc. Roy. Soc. Lond. A* **297**, 459.
- MILES, J. W. 1976 Nonlinear surface waves in closed basins. *J. Fluids Mech.* **75**, 419–448.
- MILES, J. W. 1993 On Faraday waves. *J. Fluids Mech.* **248**, 671–683.
- MILES, J. W. & HENDERSON, D. 1990 Parametrically forced surface waves. *Annu. Rev. Fluid Mech.* **22**, 143–165.
- RAFFEL, M., WILLERT, C. E., WERELEY, S. T. & KOMPENHANS, J. 2007 *Particle Image Velocimetry: A practical guide*, 2nd edn. Berlin: Springer-Verlag.
- RILEY, N 2001 Steady Streaming. *Annu. Rev. Fluid Mech.* **33**, 43–65.
- SANLI, CEYDA, LOHSE, DETLEF & VAN DER MEER, DEVARAJ 2014 From antinode clusters to node clusters: The concentration-dependent transition of floaters on a standing Faraday wave. *Phys. Rev. E* **89** (5), 053011.
- STOKES, G G 1847 *On the theory of oscillatory waves*, , vol. VIII. Transactions of the Cambridge Philosophical Society.
- STOKES, G G 1851 On the Effect of the Internal Friction of Fluids on the Motion of Pendulums. *Transactions of the Cambridge Philosophical Society* **9**, 8–.
- VAN DYKE, MILTON 1982 *An album of fluid motion*. Parabolic Press Stanford.
- VEGA, J. M, KNOBLOCH, E. & MARTEL, C. 2001 Nearly inviscid Faraday waves in annular containers of moderately large aspect ratio. *Physica D* **154** (3), 313–336.
- WALLET, A & RUELLAN, F 1950 *Trajectoires internes dans un clapotis partiel*, , vol. 5. La Houille Blanche.
- WRIGHT, P H & SAYLOR, J R 2003 Patterning of particulate films using Faraday waves. *Rev. Sci. Instrum.* **74** (9), 4063.
- WU, JUNRU, KEOLIAN, R. & RUDNICK, I. 1984 Observation of a Nonpropagating Hydrodynamic Soliton. *Phys. Rev. Lett.* **52** (1), 1421–1424.